

MaNGA AGN dwarf galaxies (MAD) - II. AGN outflows in dwarf galaxies

V. Rodríguez Morales,^{*}¹ M. Mezcua,^{1,2} H. Domínguez Sánchez,^{3,4} A. Audibert,^{5,6} F. Müller-Sánchez,⁷ M. Siudek,^{1,5} and A. ErósteGUI,¹

¹ Institute of Space Sciences (ICE, CSIC), Campus UAB, Carrer de Magrans, 08193 Barcelona, Spain

² Institut d'Estudis Espacials de Catalunya (IEEC), Edifici RDIT, Campus UPC, 08860 Castelldefels (Barcelona), Spain

³ Centro de Estudios de Física del Cosmos de Aragón (CEFCA), Plaza San Juan, 1, 44001, Teruel, Spain

⁴ Instituto de Física de Cantabria, Avenida de los Castros, s/n, 39005 Santander, Cantabria, Spain

⁵ Instituto de Astrofísica de Canarias, Calle Vía Láctea, s/n, E-38205 La Laguna, Tenerife, Spain

⁶ Departamento de Astrofísica, Universidad de La Laguna, E-38206 La Laguna, Tenerife, Spain

⁷ Department of Physics and Materials Science, The University of Memphis, 3720 Alumni Avenue, Memphis, TN 38152, USA

Received XX XX, XXXX; accepted XX XX, XXXX

ABSTRACT

Context. Active Galactic Nuclei (AGN) feedback is one of the most important mechanisms in galaxy evolution. It is usually found in massive galaxies and regulates star formation. Although dwarf galaxies are assumed to be regulated by supernova feedback, recent studies show evidence for the presence of AGN outflows and feedback in dwarf galaxies.

Aims. We investigate the presence of AGN outflows in a sample of 2292 dwarf galaxies with AGN signatures drawn from the MaNGA survey. Thanks to the integral field unit data from MaNGA we are able to spatially resolve these outflows and study their kinematics and energetics.

Methods. Using the GELATO Python code, we fit the AGN-stacked spectrum of each galaxy, which is the stack of all the spaxels classified as AGN by emission line diagnostic diagrams, and in particular the [OIII] $\lambda 5007\text{\AA}$ emission line. If the galaxies show a broad [OIII] emission line component in the stacked spectrum, we run GELATO through all the spaxels that are classified as AGN in the emission line diagnostic diagrams.

Results. We find 11 new dwarf galaxies that present outflow signatures based on the presence of a broad [OIII] emission line component. Their velocity W_{80} (width containing 80% of the flux of the [OIII] $\lambda 5007\text{\AA}$ emission line) ranges from 205 to 566 km s⁻¹ and the kinetic energy rate ranges from $\sim 10^{35}$ to $\sim 10^{39}$ erg s⁻¹. Stellar processes are unlikely to explain these outflow kinetic energy rates in the case of seven dwarf galaxies. We find a correlation between the W_{80} velocity and the [OIII] luminosity and between the kinetic energy rate of the outflow and the bolometric luminosity spanning from massive to dwarf galaxies. This suggests a similar behavior between the AGN outflows in the dwarf galaxy population with those in massive galaxies.

Key words. Outflows – Dwarf galaxies – Active galactic nuclei – Feedback

1. Introduction

Although Active Galactic Nuclei (AGN) are mostly found in massive galaxies, in the late 80s Filippenko & Sargent (1989) discovered an AGN in the dwarf (stellar mass $M_* \leq 10^{10} M_\odot$) spiral galaxy NGC 4395. Nowadays, optical spectroscopy using surveys such as the Sloan Digital Sky Survey (SDSS) or the Dark Energy Spectroscopic Instrument (DESI) has allowed us to find thousands of dwarf galaxies hosting AGN (see Pucha et al. 2024). This has been mostly based on the use of emission line diagnostic diagrams such as the Baldwin, Phillips & Terlevich (BPT; Baldwin et al. 1981), which allow us to distinguish between gas ionization produced by AGN, stars or both by comparing the ratio of the narrow emission lines [OIII] $\lambda 5007/H\beta$ against [NII] $\lambda 6583/H\alpha$, [SII] $\lambda \lambda 6716, 6731/H\alpha$ or [OI] $\lambda 6300/H\alpha$ (Kauffmann et al. 2003; Kewley et al. 2001, 2006). AGN in massive galaxies often exhibit a broad H α or H β component originating from dense gas clouds in the broad-line region (BLR) located a few parsecs from the supermassive black hole (SMBH; $M_{\text{BH}} > 10^6 M_\odot$). These clouds are ionized

by continuum emission from the accretion disk of the SMBH. In massive galaxies the typical Full Width at Half Maximum (FWHM) of the broad component ranges from ~ 1000 to ~ 5000 km s⁻¹ (Osterbrock & Ferland 2006; Kollatschny & Zetzl 2013). In dwarf galaxies such broad components have also been identified but with a less pronounced width of ~ 500 - 1000 km s⁻¹ (e.g. Reines et al. 2013; Chilingarian et al. 2018). Assuming that the gas producing the broad emission line is moving in circular orbits in the BLR around the SMBH, a BH mass measurement can be obtained from the detection of broad Balmer lines. In the case of dwarf galaxies, this BH mass is typically of $M_{\text{BH}} = 10^5 - 10^6 M_\odot$, thus lower than that of SMBHs (e.g. Greene & Ho 2007; Reines et al. 2013; Moran et al. 2014; Baldassare et al. 2015; Marleau et al. 2017; Chilingarian et al. 2018; Mezcua & Domínguez Sánchez 2020, 2024; Salehirad et al. 2022).

BPT diagnostic diagrams used in surveys that only obtain the spectrum at the center of the galaxy can miss AGN in galaxies with a high star formation rate (SFR) that dilutes the AGN signatures or in which the AGN is displaced from

* E-mail: victorproyecto98@gmail.com

the center of the galaxy (Comerford & Greene 2014). This displacement is expected to occur in approximately $\sim 50\%$ of dwarf galaxies (e.g. Bellovary et al. 2019). This problem can be solved by observing galaxies at X-ray and radio bands (e.g. Hasinger 2008; Mezcua et al. 2016, 2018, 2019; Hickox & Alexander 2018; Reines et al. 2020; Birchall et al. 2020; Bykov et al. 2024). Alternatively, integral field unit (IFU) spectrographs allow us to identify these ‘hidden AGN’ because they provide information spaxel by spaxel (i.e. we have a spectrum for each pixel of the galaxy) thanks to the different fibers arranged of each IFU (e.g. Ricci et al. 2014; da Silva et al. 2017; Wylezalek et al. 2020; Liu et al. 2020; Mezcua & Domínguez Sánchez 2020, 2024). Then, by doing spatially-resolved emission line diagnostic diagrams (i.e. BPT spaxel by spaxel) we are able to identify which regions of the galaxy are ionized by AGN or star-formation (SF) (e.g. Mezcua & Domínguez Sánchez 2020, 2024; Wylezalek et al. 2020).

AGN release energy in the form of radiation or of mechanical radio plasma coming from the gravitational energy of the material accreted by the BH. There are different launching mechanism, such as collimated jets of charged particles, winds formed from the radiation pressure or from the accretion disk. These winds rise up to outflows when they interact with and swept up material from the interstellar medium (Harrison & Ramos Almeida 2024). Outflows can also be produced by SF processes (e.g. Arce et al. 2006; Gatto et al. 2017; Romano et al. 2023; Sau et al. 2023) and can be identified by looking for broadened or shifted components in emission lines like [OIII] $\lambda 5007$, [NII] $\lambda 6583$ or [SII] $\lambda\lambda 6716, 6731$ (e.g. Holt et al. 2008; Liu et al. 2013; Harrison et al. 2014; Leung et al. 2019; Wylezalek et al. 2020). By combining the kinematic information of the emission lines with the BPT diagram diagnostics to access the gas excitation, we can have a powerful way to infer the origin of the outflow: AGN or SF processes.

The impact of AGN outflows on the host galaxy, known as AGN feedback, plays a role in regulating the star formation due to the injection of energy and the momentum transfer in the interstellar medium of the galaxy. As a result, the growth of SMBHs is interconnected with the evolution of their host galaxies, a phenomenon referred to as BH-galaxy co-evolution (e.g. Kormendy & Ho 2013; Zhuang & Ho 2023; Capelo et al. 2024). AGN feedback and outflows are typically found in massive galaxies, and they are generally suggested to prevent gas from cooling and to redistribute it (e.g. Croton et al. 2006; Bower et al. 2006; Falceta-Gonçalves et al. 2010). Nevertheless, high spatial resolution observations and recent simulations have made the understanding of AGN feedback more complex, pointing out the importance of the initial conditions in different factors, such as the gas distribution or the coupling between the outflow and the interstellar medium (e.g. Tanner & Weaver 2022, Clavijo-Bohórquez et al. 2024, see Harrison & Ramos Almeida 2024 for a recent review).

In the low-mass regime the presence of AGN outflows is a matter of debate. AGN are typically fainter and less powerful in dwarf galaxies than in massive galaxies (but see Mezcua et al. 2023, Mezcua et al. 2024). Furthermore, star formation in dwarf galaxies is commonly assumed to be regulated by stellar winds coming from supernovae (SNe). Yet, recent studies show evidence for the presence of AGN outflows and feedback in dwarf galaxies. Penny et al. (2018) found evidence for AGN feedback in a subset of 69 quenched low-mass galaxies selected

from the first two years of the SDSS MaNGA (Mapping Nearby Galaxies at Apache Point Observatory, Bundy et al. 2015) survey. Manzano-King et al. (2019) reported the detection of six dwarf galaxies selected from SDSS that have an outflow component in the [OIII] doublet with emission lines ratios consistent with AGN ionization. Liu et al. (2020) used a sample of eight dwarf galaxies with known AGN taken from Manzano-King et al. (2019), and the IFU data reveals signs of outflowing gas in seven of them based on the detection of a wing in the Gaussian fit of the [OIII] line. Liu et al. (2024) study three far-ultraviolet dwarf galaxies. They reported a fast outflow detected in multiple transitions in one source. In another source they detect a blueshifted [HeII] $\lambda 1640\text{\AA}$ emission line, likely tracing a highly-ionized AGN outflow. Zheng et al. (2023) detect an escaping outflow in a dwarf galaxy with an intermediate-mass black hole (IMBH, $100M_{\odot} \leq M_{\text{BH}} \leq 10^6 M_{\odot}$) and study the importance of the feedback by comparing the size of the outflow with the extended narrow line region. Wang et al. (2024) report a low-mass galaxy at redshift $z=3.1$ with AGN signatures, and with an absorption feature in the wings of [HeI] $\lambda 10839\text{\AA}$ indicating an ionized gas outflow. Salehirad et al. (2024) report 11 AGN dwarf galaxies with fast outflows consistent with an AGN-driven origin.

On the theoretical side, cosmological simulations considering AGN feedback in high-redshift dwarf galaxies indicate that BHs can provide a significant amount of feedback that can quench SF (Barai & Dal Pino 2018). Contrarily, Trebitsch et al. (2018) find that even in the most extreme BH growth scenario, SNe feedback quenches the AGN feedback, being this last one negligible in comparison. In recent simulations, Koudmani et al. (2022) find a midpoint where a more moderate SNe feedback in combination with an efficient AGN could be an alternative. In this simulation a variety of outcomes are obtained depending on the accretion model: from no additional suppression to moderate regulation of SF to catastrophic quenching. Arjona-Galvez et al. (2024) investigate magneto-hydrodynamical simulations of the formation of dwarf galaxies, one with AGN feedback and the other with the AGN feedback turned off. The AGN runs reproduce satisfactorily several scaling relations and they find that the global SF of galaxies with AGN is reduced compared to those galaxies in which the AGN has been turned off. At this point, different cosmological simulations bring different results, so observational constraints are needed. Local dwarf galaxies have presumably not experimented a significant evolution and thus resemble those first galaxies formed in the early Universe ($z \sim 12$). Therefore, understanding feedback processes and their contribution in dwarf galaxies could be an essential key for cosmological models of galaxy evolution.

In this paper we present a new sample of 11 dwarf galaxies with AGN outflow candidates drawn from the final MaNGA data release (DR17)¹. We compare their properties with those of massive galaxies with AGN-driven outflows. The paper is organised as follows: in Sect. 2, we study a sample of 2292 dwarf galaxies from Mezcua & Domínguez Sánchez (2024) that present AGN ionisation signatures in the spatially-resolved BPTs. We analyse the [OIII] $\lambda 5007\text{\AA}$ line in the stacked spectrum, followed by the individual spaxels, to detect and spatially resolve the outflows. In Sect. 3 we derive the extension of the outflows and study their kinematic and energetic

¹ <https://www.sdss4.org/dr17/manga/>

properties and discuss their AGN origin. Final conclusions are drawn in Sect. 4. Throughout the paper a standard Λ CDM cosmology is adopted with $H_0 = 70 \text{ km s}^{-1} \text{ Mpc}^{-1}$, $\Omega_M = 0.3$ and $\Omega_\Lambda = 0.7$.

2. SAMPLE AND ANALYSIS

2.1. Sample of dwarf galaxies in MaNGA

The sample studied in this paper is drawn from Mezcua & Domínguez Sánchez (2024). They make a selection of 3306 dwarf galaxies ($M_* \leq 10^{10} M_\odot$) from the MaNGA DR17, which is the final MaNGA data release that includes IFU observations and data products of more than 10000 nearby galaxies. Each IFU is composed of tightly-packed arrays of 19 to 127 optical fibers with diameters from 12 to 32 arcsec. It covers a wavelength range of 3600-10000Å with a spectral resolution of $R \sim 2000$.

Mezcua & Domínguez Sánchez (2024) made a pioneering classification of the spaxels of the 3306 dwarf galaxies based on the [NII]-BPT, [SII]-BPT and [OI]-BPT diagrams using the Kauffmann et al. (2003) classification cutoff, the Kewley et al. (2001) and the Kewley et al. (2006) maximum starburst lines. They combine this classification with the WHAN diagram, used to distinguish between emission by AGN or by hot old stars (Cid Fernandes et al. 2010). This yields 2292 dwarf galaxies with strong AGN ionization signatures (i.e. more than 20 spaxels with a signal-to-noise ratio (SNR) ≥ 3) classified as AGN, SF-AGN (i.e. SF in the [NII]-BPT but AGN in the [SII]-BPT or [OI]-BPT), Composite, or LINER². For a detailed description see Mezcua & Domínguez Sánchez (2024).

For all these 2292 dwarf galaxies, Mezcua & Domínguez Sánchez (2024) stack the spectrum of those AGN spaxels. The stacking procedure is described in Appendix A in Mezcua & Domínguez Sánchez (2020). In this paper, the stacked spectrum of these galaxies is fitted using GELATO (Hviding et al. 2022), available on Zenodo³. GELATO is a Python code designed to retrieve the kinematics and line fluxes of optical spectra. It fits multiple components to lines with complex kinematics and allows the user to tie parameters between emission lines (e.g. $H\alpha$ and $H\beta$ velocity dispersion or the flux ratio between [OIII] $\lambda\lambda 5007$, 4959Å emission lines which are known due to the transition probabilities). In order to run GELATO, the spectral flux, the wavelength, the inverse-variance (ivar), and the redshift (taken from the NASA-Sloan Atlas (NSA) catalogue⁴) must be provided in addition to the emission lines to be fitted, which are: [SII] $\lambda\lambda 6716$, 6731Å, [NII] $\lambda\lambda 6583$, 6548Å, $H\alpha\lambda 6563$ Å, [OI] $\lambda\lambda 6300$, 6364Å, HeI $\lambda 5876$ Å, [OIII] $\lambda\lambda 5007$, 4959, 4364Å, $H\beta\lambda 4861$ Å, [H γ] $\lambda 4340$ Å, [NeIII] $\lambda 3869$ Å, and [OII] $\lambda\lambda 3726$, 3728Å. GELATO models the stellar component using the Extended MILES stellar library (Vazdekis et al. 2016) combining Simple Stellar Populations (SSP). An additional power-law component is added if the continuum model passes a statistical F-Test at a 3σ level, corresponding to a likelihood of $\sim 99.87\%$ (Hviding et al. 2022). Additional components are also tested with an F-Test at a 3σ level and the final model is the one with the lowest Akaike Information Criteria (AIC; Akaike 1974), which is an estimator of the relative quality of

statistical models. We allow GELATO to fit a broad component to the Balmer lines and an outflow component to the [OIII] emission line, apart from the narrow component (all of them fitted as Gaussians). The distinction between broad and outflow component is based on the bounds of the dispersion and redshifts of these components. For the outflow component the dispersion has a lower value of 100 km s^{-1} and an upper value of 750 km s^{-1} corresponding to 1 and 99 percentile values of the dispersion of the second [OIII] component (Mullaney et al. 2013, for further details see Hviding et al. 2022). In this paper we use the terms ‘broad component’ and ‘outflow component’ indistinctly.

Once the stacked spectrum of each of the 2292 galaxies is fitted, the [OIII] $\lambda 5007$ Å emission line is examined to determine if a broadened or shifted component is observed (see Fig. 1), indicating gas with different kinematics than the rest of the ionized gas in the galaxy and thus potentially tracing outflowing gas (e.g. Liu et al. 2013; Manzano-King et al. 2019). Furthermore, a visual inspection is done to remove those galaxies in which GELATO associated a broad component due to the noise near the [OIII] $\lambda 5007$ Å line. Since the final model is the one with the lowest AIC, a more complex model might be selected unnecessarily. To address this, we check in how many stacked spectra the [OIII] lines present a better fit with a double Gaussian rather than a single Gaussian comparing the χ^2 value of both fits and doing a second visual inspection. If the double Gaussian fit has $\chi^2 \leq 20$ and it improves by at least 20% the χ^2 of the single fitting, the galaxy is included in our sample of outflow candidates (e.g. Hao et al. 2005; Reines et al. 2013). At this point, the number of AGN dwarf galaxies which fulfill our criteria to show outflows signatures is 64.

To further restrict our sample of dwarf galaxies with possible AGN outflows, we perform a similar analysis as the one explained above, but now for the individual AGN spaxels of the 64 candidates selected. We take advantage of the MaNGA Data Reduction Pipeline (DRP)⁵ of DR17 data-products, which provide flux calibrated, sky subtracted, coadded data cubes from each of the individual exposures for a given galaxy. The wavelength, flux and ivar of each spaxel is provided by the LOGCUBE data cube. Only spaxels with a SNR ≥ 10 are selected in order to avoid unreliable spectrum fittings (in Appendix A a discussion of the SNR threshold selection can be found). After running GELATO for each of the individual spaxels of the 64 dwarf galaxies with AGN outflow candidates, we select only those galaxies that present more than 10 consecutive AGN spaxels with a broad component in the [OIII] line ($n_{\text{out}} > 10$) in at least one region of the host galaxy. By applying this cut, a final sample of 11 dwarf galaxies with AGN outflow candidates is obtained, of which five are classified as AGN galaxies and six as SF-AGN according to Mezcua & Domínguez Sánchez (2024). Two of the AGN dwarf galaxies (8982-3703 and 9889-1902) show additional evidence for the presence of AGN based on the detection of radio emission and one (10223-3702) based on its mid-infrared colors according to Jarrett et al. (2011) or Stern et al. (2012) criteria. The analysis of the individual spaxels is also performed for the SF spaxels of these 11 dwarf galaxies in order to discuss the origin of the outflow (see Sect. 3.4).

² Low Ionization Emission Line Region (LINER)

³ <https://zenodo.org/records/5831730>

⁴ <http://nsatlas.org/data>

⁵ <https://www.sdss4.org/dr17/manga/manga-data/data-access/>

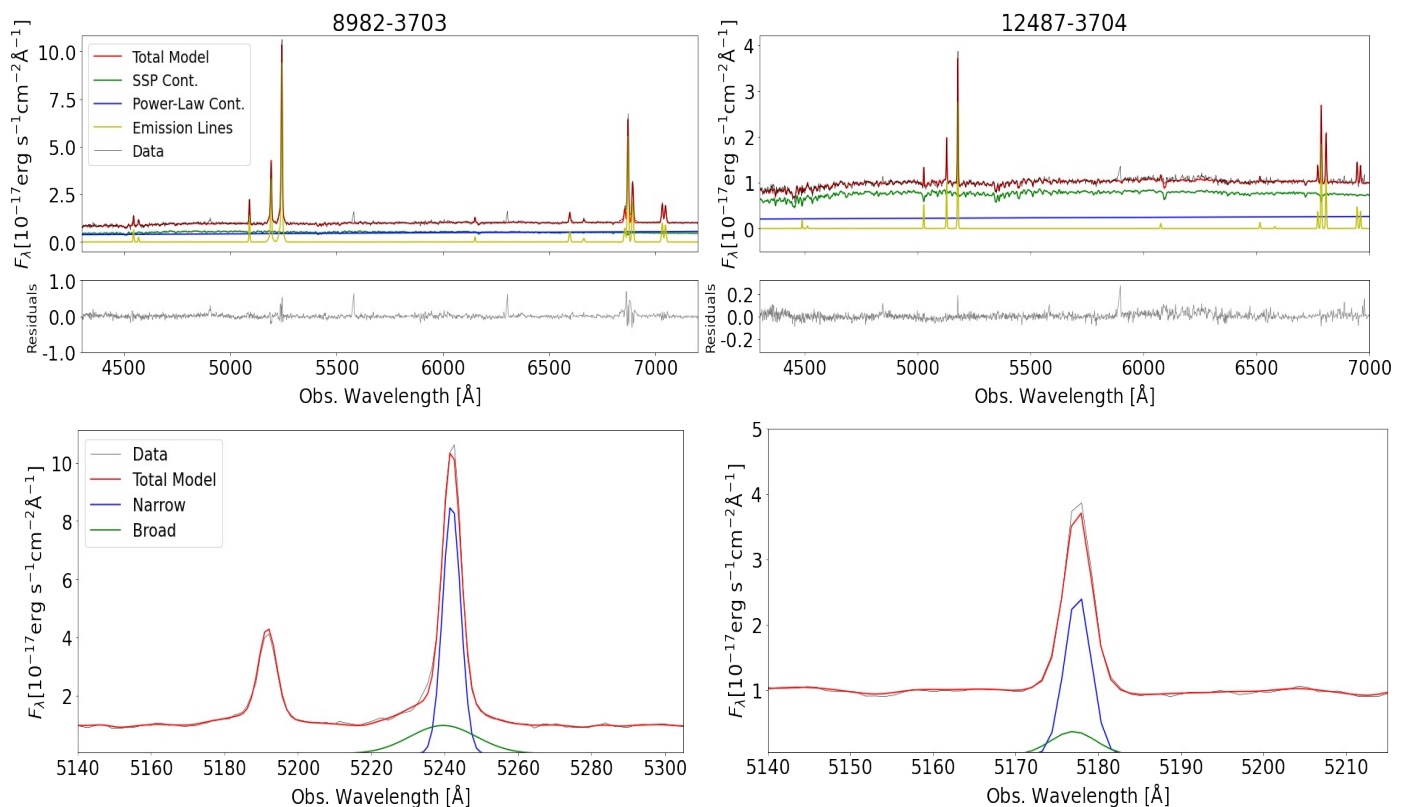


Fig. 1: **Top left and right:** Spectra of the galaxies 8982-3703 and 12487-3704, respectively. The dark line is the stacked spectrum of the AGN spaxels. The green line is the best fit of the stellar continuum combining SSPs. The blue line is an additional power-law component, the yellow line represents the fitted emission lines and the red line is the sum of all these components that make the total model. The residuals after subtraction of the total model from the data are shown at the bottom. **Bottom left and right:** Zoom-in to the $[\text{OIII}]\lambda 5007\text{\AA}$ doublet region of the stacked spectrum. The $[\text{OIII}]$ line is fitted by a narrow (blue) and a broad (green) component.

2.2. Star formation rate measurement

We fit spectral energy distributions (SED) using Code Investigating GALaxy Emission (CIGALE; Boquien et al. 2019) to estimate the SFR of the 11 MaNGA dwarf galaxies with AGN outflows candidates, as the one obtained by taking the $\text{H}\alpha$ emission line from the MaNGA data-analysis pipeline (DAP; Westfall et al. 2019; Belfiore et al. 2019) does not account for AGN contribution (see Sect. 3.4.1). We consider Bruzual & Charlot (2003) single stellar populations models assuming a Chabrier initial mass function Chabrier (2003). We use the standard nebular emission model from Inoue (2011) and the dust attenuation model using the Calzetti et al. (2000) starburst attenuation curve. The reprocessed dust emission is modeled using the Draine et al. (2013) dust models. Finally, we use the AGN emission model from Fritz et al. (2006). We use, when available, the following photometry: SDSS magnitudes in the optical/infrared bands (u,g,r,i,z; Fukugita et al. 1996; Doi et al. 2010) adapted to a composite model following Maraston et al. (2013). Near-infrared photometry in the J ($1.25\mu\text{m}$), H ($1.65\mu\text{m}$), and K ($2.17\mu\text{m}$) bands from The Two Micron All Sky Survey (2MASS; Cutri et al. 2003, 2012; Skrutskie et al. 2006). Infrared photometry from the Wide-field Infrared Survey Explorer (WISE; Wright et al. 2010; Cutri et al. 2021) passbands W1, W2, W3 and W4 with effective wavelength 3.4, 4.6, 12.1 and $22.5\mu\text{m}$. Finally, far- and near-ultraviolet measurements are also included from the Galaxy Evolution Explorer (GALEX; Bianchi et al. 2011, 2017; Osborne et al. 2023).

2.3. Sample of massive galaxies in MaNGA

To compare our results with a sample of massive galaxies, we use the MaNGA sample of massive galaxies ($M_* > 10^{10} M_\odot$) with AGN outflows of Wylezalek et al. (2020). To ensure that the analysis is carried out in the same way for both dwarf and massive galaxies, we perform the same analysis as for the dwarf galaxies described in Sect. 2.1 for the 154 massive galaxies with AGN from Wylezalek et al. (2020). We find that 46 out of these 154 massive galaxies present an extended broad component region (10 consecutive AGN spaxels with a broad component in the $[\text{OIII}]$ line). Wylezalek et al. (2020), considering only those AGN galaxies with $W_{80} \geq 500 \text{ km s}^{-1}$ (where W_{80} is the velocity width containing 80% of the flux of the emission line), report 29 AGN outflows in their sample of massive galaxies. This cut in the W_{80} velocity is the main reason behind the difference between the number of outflows we find in their sample and those reported in Wylezalek et al. (2020). From the 46 massive galaxies with AGN outflow signatures we report, 17 have $W_{80} \geq 500 \text{ km s}^{-1}$ being 11 out of these 17 consistent with the 29 reported by Wylezalek et al. (2020). For the remaining 18 galaxies with $W_{80} \geq 500 \text{ km s}^{-1}$ reported by Wylezalek et al. (2020), we find, according to our measurements (see Sect. 3.1), that 6 of them have $W_{80} \leq 500 \text{ km s}^{-1}$ and the rest does not meet our criteria on consecutive AGN spaxels with a broad component in the $[\text{OIII}]$ emission line.

3. Results and discussion

In this work, we report the discovery of 11 MaNGA dwarf galaxies with AGN outflow candidates identified using the MaNGA survey. Furthermore, we investigate whether the gas kinematics differs from that of the stellar kinematics. Although gas and stars can rotate perpendicularly (Sarzi et al. 2006), the misalignment may suggest past interactions (Casanueva et al. 2022; Raimundo et al. 2023; Zinchenko 2023; Winiarska et al. 2025) or the presence of potential outflows (Ristea et al. 2022). To do this, the position angle (PA) of the [OIII] total gas velocity and of the stellar velocity is derived using the PaFit package in Python (Krajinovic et al. 2006; see Table 1). For 8 out of the 11 dwarf galaxies with outflows signatures, we find that the $|\text{PA}_{\text{gas}} - \text{PA}_{\text{stars}}| \gtrsim 20^\circ$, supporting a deviation of the gas from the stellar kinematics (see Figs. 2 and 3). The remaining 3 galaxies, 7992-6102, 8657-6104 and 9889-1902 (which is in a merger process), have a PA difference $\leq 6^\circ$, which cannot confirm the outflowing nature of the gas.

In the following sub-sections we present the outflow kinematic and energetic properties of the 11 MaNGA dwarf galaxies. We start with the calculation of the velocity of the outflows, followed by the radius, the mass and the energy, momentum and mass rates.

3.1. Outflow velocity and radius

The outflow velocity is defined in Manzano-King et al. (2019) as:

$$v_{\text{out}} = -v_0 + \frac{W_{80}}{2} \quad (1)$$

where v_0 is the velocity offset between the narrow and the broad component of the [OIII] $\lambda 5007\text{\AA}$ line. In the case of a single Gaussian fitting, W_{80} could be defined as $W_{80} = 1.09 \times \text{FWHM}$. However, for non-Gaussian emission line profiles, the non-parametric velocity width measurements are more sensitive to the weak broad bases (Liu et al. 2013). As our fitting is composed by the sum of two Gaussians, W_{80} is calculated using the following expression:

$$W_{80} \equiv v_{90} - v_{10} \quad (2)$$

where v_{90} and v_{10} are the velocities at the 10th and 90th percentiles of the total flux. In order to calculate these velocities, we need to calculate the cumulative flux as a function of the velocity:

$$\phi(v) \equiv \int_{-\infty}^v F_v(v') dv' \quad (3)$$

The total line flux is given by $\phi(\infty)$. F_v is the spectral flux density. In the wavelength space the spectral flux density can be parameterized as a Gaussian distribution:

$$F_\lambda = \frac{F}{\sigma_\lambda \sqrt{2\pi}} \exp\left(-\frac{1}{2} \left(\frac{\lambda - \lambda_r(1+z)}{\sigma_\lambda}\right)^2\right) \quad (4)$$

taking into account the expansion of the Universe with the factor $(1+z)$. F is the integrated line flux, λ is the wavelength,

MaNGA plateifu (1)	PA _{gas} (°) (2)	PA _{stars} (°) (3)	PA _{gas} - PA _{stars} (°) (4)
10223-3702	112	143	31
10226-1901	118	56	62
11022-12702	124	149	25
11754-3701	44	25	19
11826-12702	119	142	25
12487-3704	149	62	87
7992-6102	142	136	6
8655-6101	93	68	25
8657-6104	12	12	0
8982-3703	56	6	50
9889-1902	118	118	0

Table 1: **Column designation:** (1) MaNGA plateifu; (2) position angle of the [OIII] gas; (3) position angle of the stellar component; (4) difference between the gas and stellar position angle.

λ_r is the wavelength of the emission line in the rest-frame and σ_λ is the dispersion in units of wavelength. As the dispersion of the line is dominated by the kinematics of the gas, we convert σ_λ into velocity units by using the Doppler effect:

$$\sigma = c \frac{\sigma_\lambda}{\lambda_r(1+z)} \quad (5)$$

Notice that the integrand in Eq.3 is in the velocity space. By definition $F_v dv = F_\lambda d\lambda$ meaning that $\int F_\lambda d\lambda = \int F_v dv$ as long as the bounds of integration are properly adjusted. As $1+z = 1+v/c = \lambda/\lambda_r$ it implies that $d\lambda/dv = \lambda_r/c$.

In the case of a double Gaussian fitting, F_v will be the sum of both Gaussian components: the narrow and the broad. GELATO outputs σ and F , so we can calculate W_{80} and v_{out} . A map showing the spatial distribution of the outflow velocity (in terms of W_{80} and v_{out}) is shown for two of the 11 dwarf galaxies with AGN outflow candidates (Figs. 2 and 3). In Table 2 the results are summarized by taking the median of all the AGN spaxels with outflow signatures.

There are two different scenarios for calculating the outflow radius: when the full extent of the outflow is not observed (Fig. 2) and when it is observed (Fig. 3). For each of these two cases a different criteria is adopted:

- If it is fully extended: we consider that the diameter is the largest distance of consecutive AGN spaxels with outflow signatures.
- If it is not fully extended: We consider the radius as the distance from the central spaxel to the further AGN spaxel with outflow signature that is in a region with at least 10 consecutive AGN spaxels with outflow signatures.

As each spaxel is 0.5 arcsec size, the angular size of the outflow can be calculated, and through parallax, the projected radius is obtained:

$$R_{\text{out}} = \tan(\alpha) d_l \quad (6)$$

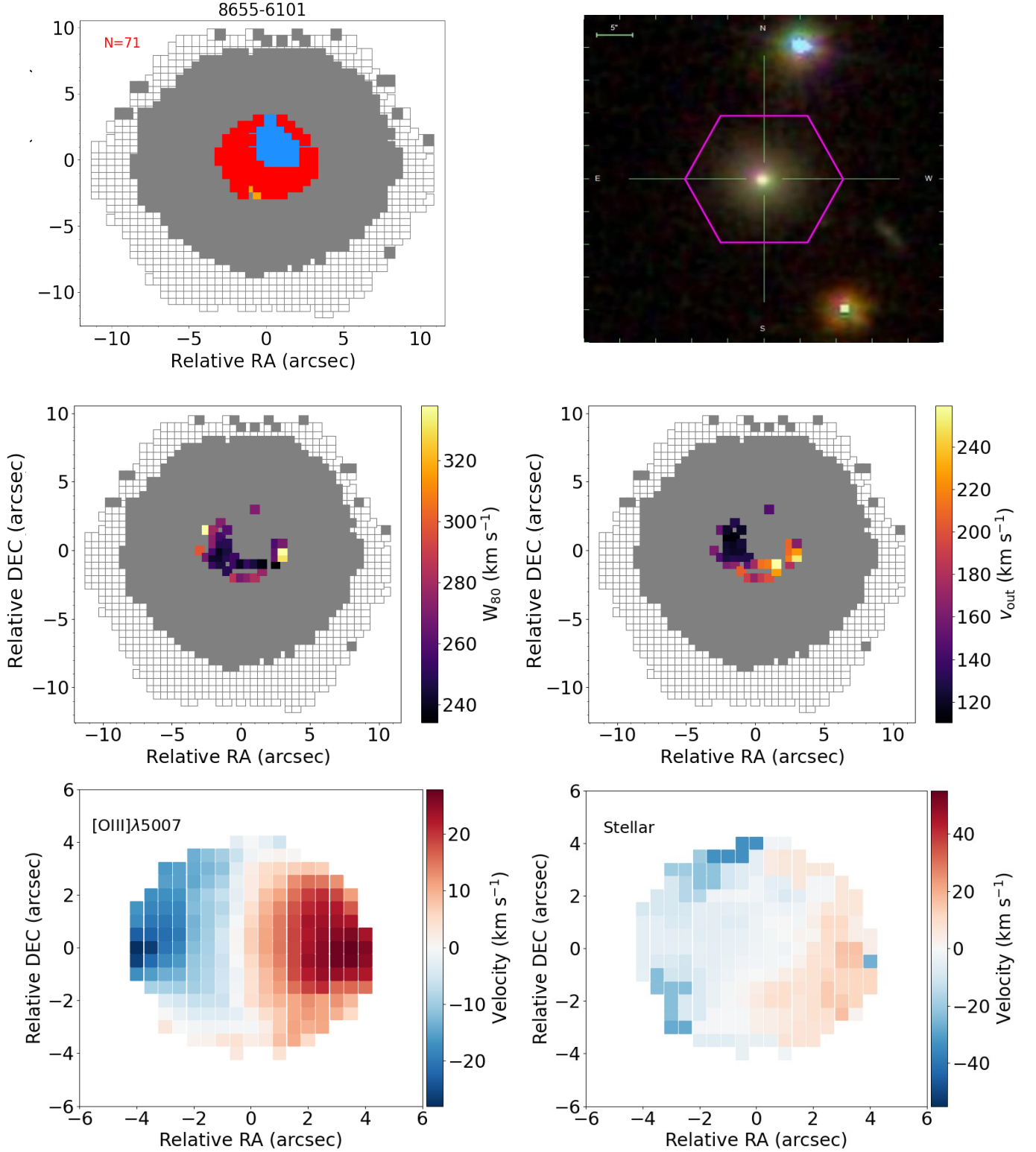


Fig. 2: MaNGA analysis for one of the dwarf galaxies with AGN outflow candidates (8655-6101). **Top left:** Spatial distribution of the BPT-classified spaxels (red: AGN; green: Composite; blue: SF; Orange: LINER). The ‘N’ shows the number of AGN spaxels used in the analysis (see Sect. 2). **Top right:** SDSS composite image. The pink hexagon shows the IFU coverage. **Middle:** Spatial W_{80} (left) and v_{out} (right) outflow velocity distribution, in which we can see the extension of the outflow. Empty squares mark the IFU coverage and grey squares those spaxels with continuum SNR > 1. **Bottom:** MaNGA $[\text{OIII}]\lambda 5007\text{\AA}$ velocity map (left) and stellar velocity (right).

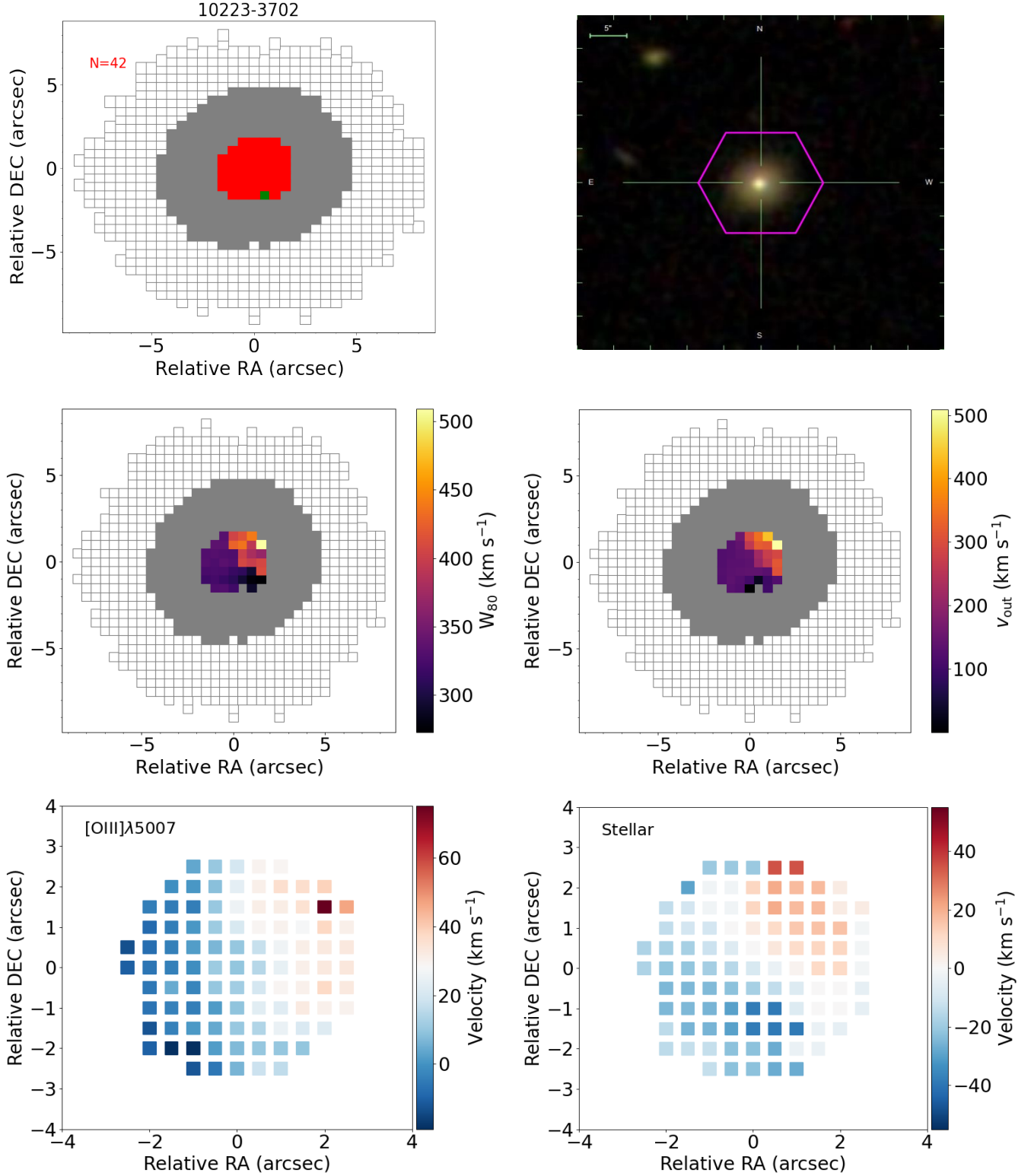


Fig. 3: Same caption as in Fig. 2 for the dwarf galaxy 10223-3702.

where α is half of the angular size in radians and d_l is the luminosity distance. We use the projected radius as a lower limit of the outflow radius, since the physical size depends on the inclination angle of the outflow with respect to the line of sight.

3.2. Energetics of the outflow

The ionized gas mass of the outflow can be calculated based on the luminosity of the H α emission line. Considering the sum of

all the AGN spaxels with outflow signatures and the equation defined by Osterbrock & Ferland (2006), we have:

$$M_{\text{out}} = \sum_{i=1}^{n_{\text{out}}} m_{\text{out}} = \sum_{i=1}^{n_{\text{out}}} 4.48 M_{\odot} \left(\frac{L_{H\alpha}}{10^{35} \text{erg s}^{-1}} \right) \left(\frac{\langle n_e \rangle}{1000 \text{cm}^{-3}} \right)^{-1} \quad (7)$$

where M_{out} is the total mass of the outflow, m_{out} is the outflow mass within individual spaxels and $L_{H\alpha}$ is the $H\alpha$ luminosity of the individual outflow spaxels. Focusing on those spaxels with outflow, the electron density, n_e is estimated using the $[\text{SII}]\lambda 6716\text{\AA}/[\text{SII}]\lambda 6732\text{\AA}$ relation (Sanders et al. 2015):

$$n_e(R) = \frac{cR - ab}{a - R} \quad (8)$$

where R is the ratio between the $[\text{SII}]$ emission lines flux and a , b and c are dimensionless constants equal to 0.4314, 2.107 and 627.1 respectively. The electron density ranges from $825 \text{ cm}^{-3} < n_e < 1071 \text{ cm}^{-3}$.

As the detected outflows are spatially resolved, the mass (dM/dt), momentum (dP/dt), and kinetic energy (dE/dt) rates can be calculated using the following equations (e.g. Liu et al. 2020; Bohn et al. 2021):

$$dM/dt = \sum_{i=1}^{n_{\text{out}}} dm/dt = \sum_{i=1}^{n_{\text{out}}} \frac{m_{\text{out}} v_0 \sec \theta}{R_{\text{out}}} \quad (9)$$

$$dP/dt = \sum_{i=1}^{n_{\text{out}}} (v_0 \sec \theta) dm/dt \quad (10)$$

$$dE/dt = \frac{1}{2} \sum_{i=1}^{n_{\text{out}}} [(v_0 \sec \theta)^2 + 3\sigma_{\text{out}}^2] dm/dt \quad (11)$$

where v_0 here is the absolute value of the velocity offset between the narrow and broad component (see Eq. 1), σ_{out} is the velocity dispersion measured from the outflow component within individual spaxels and $\theta = \sin^{-1}(r_{\text{spaxel}}/R_{\text{out}})$, where r_{spaxel} is the angular size of the spaxel converted into physical distance. The results of the mass, momentum and kinetic energy rate range from $10^{-4.4} < dM/dt (M_{\odot} \text{yr}^{-1}) < 10^{-1.2}$, from $10^{4.3} < c dP/dt (L_{\odot}) < 10^{8.6}$, and from $10^{35.4} < dE/dt (\text{erg s}^{-1}) < 10^{39.5}$, and are also listed in Table 2.

3.3. Outflows escaping their host halos

To investigate whether the outflows are able to escape the gravitational potential of their host halos, the velocity of the outflows and the escape velocity, v_{esc} are compared. Assuming a Navarro-Frenk-White profile (NFW; Navarro et al. 1997) and making use of the abundance matching (Moster et al. 2010, 2013), we infer the halo mass from the stellar mass of the galaxy:

$$\frac{M_*}{M_h} = 2 \left(\frac{M_*}{M_h} \right)_0 \left[\left(\frac{M_h}{M_1} \right)^{-\beta} + \left(\frac{M_h}{M_1} \right)^{\gamma} \right]^{-1} \quad (12)$$

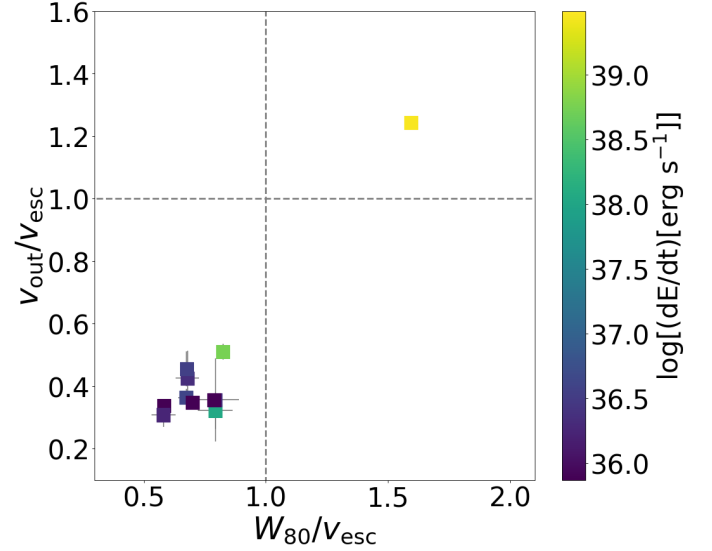


Fig. 4: A comparison of the ratios of the two velocity indicators W_{80} and v_{out} with v_{esc} . The grey dashed lines represent the 1:1 relation. One out of the 11 MaNGA dwarf galaxies with AGN outflow candidates would have outflows fast enough to become unbound from the galaxy and from its dark matter halo.

This expression has four parameters: the normalization of the stellar-to-halo mass ratio $(M_*/M_h)_0 = 0.02817$, a characteristic mass $M_1 = 10^{11.899}$, and $\beta = 0.611$, $\gamma = 1.068$, being these last two slopes an indication of the behaviour of the mass ratio at the low-mass and high-mass end, respectively. Then, a gravitational potential is considered at the center $\phi(r = 0)$ from a spherical NFW profile (Łokas & Mamon 2001):

$$\phi(r = 0) = -\frac{4}{3} c g(c) \pi G r_v^2 v_c^0 \quad (13)$$

where $c = 10$ is the concentration parameter, $g(c) = 1/(\ln(1+c) - c/(1+c))$ is a function of the concentration parameter, $v = 200$ is the virial overdensity, $\rho_c^0 = 277.5 M_{\odot}/\text{kpc}^3$ is the present critical density, and $r_v = (3M_h/4\pi v \rho_c^0)^{1/3}$ is the virial radius. Finally, using the expression defined in Manzano-King et al. (2019) we obtain the escape velocity:

$$v_{\text{esc}}^2 = 2|\phi(r = 0)| \quad (14)$$

In Fig. 4 the velocity of the outflow is compared with v_{esc} . While W_{80} is the most common value when defining the outflow velocity, v_{out} has recently been also adopted as outflow velocity estimator (e.g. Manzano-King et al. 2019; Bohn et al. 2021; Zheng et al. 2023). According to both W_{80} and v_{out} , only 8982-3703 would have outflows consistent with being fast enough to escape the galaxy and the dark matter halo. Also, in Fig. 4, we show a colorbar with the kinetic energy rate of the galaxies, being 8982-3703 the only galaxy which is able to escape the one with the highest kinetic energy rate. For 8982-3703, the outflowing gas could contribute to AGN feedback by removing gas from the central region or could cause feedback to the galactic halo by heating the intergalactic medium (Smethurst et al. 2021).

3.4. What is driving these outflows?

Although we mainly base our analysis on selecting AGN spaxels to detect AGN outflows, we go into a deeper study in order to understand the origin of the outflows detected.

3.4.1. Could stellar winds from massive stars or SNe be the driven mechanism?

Massive stars are able to inject energy and momentum to the interstellar medium through outflows coming from stellar winds and SNe explosions. These stellar processes are commonly believed to be the main source of feedback in dwarf galaxies (e.g. Veilleux et al. 2005; Martín-Navarro & Mezcua 2018). In this section, we investigate whether the 11 MaNGA dwarf galaxies with outflows could be driven by stellar processes by computing the expected energy driven by stellar wind outflows in massive stars or by SNe outflows.

For stellar winds in massive stars, the kinetic energy rate can be derived as $dE/dt = \frac{1}{2} dM/dt v_{\text{out}}^2$ (Rosen 2022), where dM/dt is the mass rate, which typically ranges from 10^{-5} to $10^{-4} M_{\odot}/\text{yr}$ (Bally 2008). The outflow velocity in massive stars rarely surpasses 100 km s^{-1} (e.g. Churchwell 1997; Commerçon et al. 2022). Consequently, the kinetic energy rate is expected to be in the range of $10^{34-35} \text{ erg s}^{-1}$, which is lower than our results, thus ruling out massive stars as the driving mechanism.

For SNe, the kinetic energy rate can be calculated as $\sim 7 \times 10^{41} (\text{SFR}/M_{\odot} \text{ yr}^{-1})$ (Veilleux et al. 2005). We calculate the SFR by taking the total $\text{H}\alpha$ and $\text{H}\beta$ emission lines from the MaNGA data-analysis pipeline (DAP; Westfall et al. 2019; Belfiore et al. 2019) and using the equation $\log(\text{SFR}) = \log(L_{\text{H}\alpha}) - 41.27$ (Kennicutt Jr & Evans 2012) after having previously corrected $L_{\text{H}\alpha}$ from extinction using the Calzetti et al. (2000) extinction law. A range of SNe kinetic energy rate that goes from $dE/dt \sim 10^{40} \text{ erg s}^{-1}$ to $\sim 10^{41} \text{ erg s}^{-1}$ is obtained. The expected SNe kinetic energy rate is one to six orders of magnitude higher than the kinetic energy rate of the 11 MaNGA dwarf galaxies with outflows. Consequently, in terms of energy, the 11 outflows detected could be driven by SNe as the kinetic energy rate of the SNe is able to explain the presence of outflows up to $10^{40-41} \text{ erg s}^{-1}$. However, the SFR might be overestimated in those cases where the AGN dominates (see Fig. 3) by the fact that the $\text{H}\alpha$ emission line comes mostly from the AGN. To overcome this problem, we derive the SFR from the SED fitting (see Sect. 2.2). The SFR obtained from the SED fitting is similar or even higher with those obtained from the $\text{H}\alpha$ emission line, this is in agreement with the results obtained from Siudek et al. (2024). Alternatively, we also use a SFR indicator based on the $[\text{OII}]\lambda 3726$ emission line ($\text{SFR}(\text{OII})$; e.g. Kennicutt Jr 1998; Hopkins et al. 2003; Kewley et al. 2004). We correct the $[\text{OII}]\lambda 3726$ emission line for extinction following Calzetti et al. (2000) extinction law and correct for AGN contribution by subtracting 10 per cent of the total $[\text{OIII}]\lambda 5007$ luminosity (Vietri et al. 2022). The $\text{SFR}(\text{OII})$ obtained is typically one order of magnitude lower than that obtained from the $\text{H}\alpha$ emission line and from the SED fitting. However, the SNe kinetic energy rate computed from the $\text{SFR}(\text{OII})$ still remains several orders of magnitude higher than the kinetic energy rate of the 11 MaNGA dwarf galaxies with outflows.

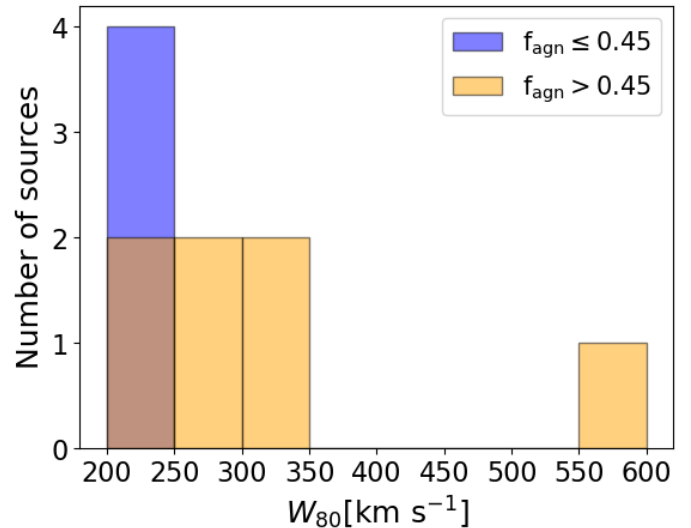


Fig. 5: Distribution of the W_{80} velocity for the dwarf galaxies with AGN outflow candidates with AGN fraction ≤ 0.45 (blue), and with AGN fraction > 0.45 (orange).

3.4.2. AGN fraction and W_{80} velocity

In this section, we look at the AGN fraction, $f_{\text{AGN}} = n_{\text{agn}}/(n_{\text{agn}} + n_{\text{SF}})$, being n_{agn} the number of spaxels classified as AGN and n_{SF} the number of spaxels classified as SF. A Mann-Whitney U test is performed to see if the W_{80} velocity of the MaNGA sample of 11 dwarf galaxies with AGN outflow candidates comes from different distributions when the AGN fraction is taken into account. We find that when the AGN fraction > 0.45 , the W_{80} velocities are drawn from a different distribution at a $\sim 99\%$ confidence level being the p-value ~ 0.006 (see Fig. 5). These velocities are higher (from 231 km s^{-1} to 566 km s^{-1}) than those corresponding to the galaxies with an AGN fraction < 0.45 (from 205 km s^{-1} to 227 km s^{-1}). Seven out of the 11 MaNGA dwarf galaxies have an AGN fraction > 0.45 , five of them classified as AGN, and two as SF-AGN (see Table 2). Therefore, since AGN outflows are expected to be faster than those driven by stellar processes (Liu et al. 2020; Wylezalek et al. 2020), the AGN emerges as the main candidate to be the driven mechanism of the outflows observed in these seven galaxies.

3.4.3. Study of the SF spaxels

We also study the detection of outflows in the SF spaxels of our sample of 11 dwarf galaxies following the same procedure for the individual spaxels as the one described in Sect. 2.1. For the six dwarf galaxies classified as SF-AGN (see Table 2), the W_{80} is consistent within the errors when comparing the SF spaxels against the AGN spaxels. On the contrary, for the five dwarf galaxies classified as AGN, three of them (10223-3702, 12487-3704 and 8982-3703) have an AGN fraction $f_{\text{AGN}} = 1$ so, although we cannot do this analysis, the absence of spaxels ionized by SF suggests that for these three galaxies the AGN must drive the outflow. The two remaining galaxies (8655-6102 and 9889-1902) present lower W_{80} velocities in the SF spaxels than in the AGN spaxels, even when accounting for their errors. This indicates that for these two galaxies the AGN could be the

main candidate for driving the outflows.

Regarding the kinetic energy rate we find consistent values, within the errors, for those obtained from SF spaxels compared to those obtained from AGN spaxels. However, for the galaxy 9889-1902, the kinetic energy rate calculated from the AGN spaxels is one order of magnitude higher. This makes 9889-1902 a strong candidate for hosting AGN outflows, as they are expected to be more energetic than SF outflows (Aravindan et al. 2023).

3.4.4. AGN bolometric luminosity and kinetic energy rate

The AGN bolometric luminosity (L_{bol}) is given by $L_{\text{bol}} = 1000 \times L_{[\text{OIII}]}$ (Moran et al. 2014), where $L_{[\text{OIII}]}$ is the sum of the $[\text{OIII}]\lambda 5007$ luminosities of those spaxels classified as AGN or Composite in the BPT diagrams (Mezcua & Domínguez Sánchez 2024). The AGN bolometric luminosity L_{bol} for the 11 MaNGA dwarf galaxies with AGN outflow candidates (see Table 3), is four to six orders of magnitude higher than the kinetic energy rate of the outflow, implying that the AGN in these 11 galaxies are capable of driving these outflows (Liu et al. 2020).

Recapitulating: the five MaNGA dwarf galaxies classified as AGN are more likely to have outflows driven by the AGN, as indicated by their AGN fraction being higher than that of the six dwarf galaxies classified as SF-AGN, their L_{bol} being greater than the kinetic energy rate, and a higher W_{80} velocity in the AGN spaxels than in the SF spaxels. In the case of the six MaNGA dwarf galaxies classified as SF-AGN, two (10226-1901 and 11754-3701) have an AGN fraction and W_{80} consistent with being drawn from the same distribution as the five AGN galaxies. For the remaining four SF-AGN it is difficult to distinguish the driving mechanism of the outflow being both SNe and AGN possible candidates.

At this point, we divide the sample of 11 MaNGA dwarf galaxies with AGN outflow candidates in two sub-samples: seven MaNGA dwarf galaxies consistent with AGN outflows (the five AGN and two SF-AGN: 10226 and 11754-3701) and four MaNGA dwarf galaxies with uncertain outflows (the remaining four SF-AGN). We emphasize that for all the 11 dwarf galaxies, we cannot rule out the possibility of SNe being the driving mechanism as the SNe kinetic energy rate exceeds the outflow kinetic energy rate in all cases.

3.5. Mass-loading factor

The mass-loading factor is a parameter used to compare the amount of gas that is ejected by the outflow to that consumed by SF (Harrison & Ramos Almeida 2024). It is defined as the ratio of the outflow mass rate compared with the SFR, $\eta = (dM/dt)/\text{SFR}$. In the MaNGA sample of seven dwarf galaxies with AGN outflows we find that the mass-loading factor for all of them is $\eta \ll 1$ for all three SFR indicators: the one obtained from the $\text{H}\alpha$ emission line, the one derived from SED fitting, and the SFR(OII). This implies that the amount of gas used for SF processes is greater than the one ejected by the outflow, being these outflows unlikely to quench the SF in the host galaxy (Carniani et al. 2024). However, the mass-loading factor can be misleading due to the fact that the spatial scale when calculating the energetic properties of the outflows and the one

to obtain the integrated SFR are different: few kiloparsec scales vs galaxy scales (Harrison & Ramos Almeida 2024), except for the galaxies 11754-3701 and 11826-12702 in which $R_{\text{out}} > 5$ kpc.

3.6. Comparison with other works on dwarf galaxies

In this section we compare the outflow velocity (as v_{out} and W_{80}) and luminosity obtained for the sample of 11 MaNGA dwarf galaxies with AGN outflow candidates with other studies. For the seven MaNGA dwarf galaxies with AGN outflows the W_{80} velocity ranges from 231 to 566 km s^{-1} and v_{out} from 107 to 441 km s^{-1} . In the case of 9889-1902 and 7992-6102 their values of W_{80} (333 km s^{-1} and 226 km s^{-1} , respectively) and v_{out} (206 km s^{-1} and 120 km s^{-1} , respectively) could be enhanced due to the merger process in which they are involved. For the four MaNGA dwarf galaxies with uncertain outflows the W_{80} ranges from 205 to 226 km s^{-1} and v_{out} from 96 to 132 km s^{-1} . These results are compared with those of other dwarf galaxies with AGN outflow candidates. By using IFU spectroscopy, Liu et al. (2020) study 8 out of the 29 dwarf galaxies previously studied in Manzano-King et al. (2019) using longslit spectroscopy. The authors detect AGN outflows with W_{80} ranging 140-980 km s^{-1} considering a $[\text{OIII}]\lambda 5007\text{\AA}$ line profile with up to three Gaussians components (i.e. C1, C2 and C3), where C2 and C3 show strong evidence of outflows. Bohn et al. (2021) also studied the same sample as Manzano-King et al. (2019) but focusing on the $[\text{Si VI}] 1.9630\mu\text{m}$ line instead of the $[\text{OIII}]\lambda 5007\text{\AA}$ and obtaining an outflow velocity range $155 \leq v_{\text{out}} (\text{km s}^{-1}) \leq 770$ and $108 \leq W_{80} (\text{km s}^{-1}) \leq 1350$. Zheng et al. (2023) find AGN outflow with velocity $v_{\text{out}} = 471 \text{ km s}^{-1}$ for SDSS J0228-0901. The velocities of the 11 MaNGA dwarf galaxies with AGN outflow candidates are thus consistent with those previously studied.

Regarding luminosity, the $L_{[\text{OIII}]}$ derived from the sum of the AGN and Composite spaxels is compared against works that report the total $[\text{OIII}]$ luminosity, so we must take some considerations for both dwarf and massive galaxies.

For the dwarf galaxies reported in Liu et al. (2020), the AGN spaxels contribute at least $\sim 95\%$ of the $[\text{OIII}]$ luminosity, which ranges from $\sim 10^{39} \text{ erg s}^{-1}$ to $\sim 10^{41} \text{ erg s}^{-1}$, making our results comparable. For the MaNGA sample of seven dwarf galaxies with AGN outflows, we obtain $L_{[\text{OIII}]}$ that ranges from $\sim 10^{38} \text{ erg s}^{-1}$ to $\sim 10^{41} \text{ erg s}^{-1}$. These results agree with those in Liu et al. (2020). For the four dwarf galaxies with uncertain outflows, three of them present $L_{[\text{OIII}]} \sim 10^{37} \text{ erg s}^{-1}$, which is two to four orders of magnitude lower than those from Liu et al. (2020) possibly indicating a different origin.

In the next section we compare our results with massive galaxies where the AGN dominate, assuming that the total $[\text{OIII}]$ luminosity comes mostly from the AGN.

3.7. Comparison with massive galaxies

In Fig. 6, we show the W_{80} velocity vs $L_{[\text{OIII}]}$ for: the MaNGA sample of 11 dwarf galaxies with AGN outflow candidates reported here, the dwarf galaxies with AGN outflows studied in Liu et al. (2020), the low-to-intermediate luminosity massive galaxies with AGN outflows from Wylezalek et al. (2020),

Table 2: Properties of the outflows for the MaNGA sample of 11 dwarf galaxies.

MaNGA plateifu	RA (J2000)	DEC (J2000)	z	$\log(M_*)$ (M_\odot)	SFR ($M_\odot \text{ yr}^{-1}$)	f_{AGN}	W_{80} (km s^{-1})	v_{out} (km s^{-1})	R_{out} (kpc)	$\log(M_{\text{out}})$ (M_\odot)	$\log(dM/dt)$ ($M_\odot \text{ yr}^{-1}$)	$\log(dE/dt)$ (erg s^{-1})	$\log(c \text{ dP/dt})$ (L_\odot)	Type
(1)	(2)	(3)	(4)	(5)	(6)	(7)	(8)	(9)	(10)	(11)	(12)	(13)	(14)	(15)
10223-3702	33.524643	-0.276961	0.0373	9.8	0.18	1.00	330 ± 30	134 ± 24	1.3 ± 0.4	5.00 ± 0.02	-2.38 ± 0.04	38.0 ± 0.6	7.30 ± 0.08	AGN [†]
10226-1901*	38.208904	-0.353272	0.0204	9.0	0.15	0.63	238 ± 29	107 ± 40	1.5 ± 0.3	4.09 ± 0.01	-3.7 ± 0.1	36.4 ± 0.7	5.9 ± 0.1	SF-AGN
11022-12702	219.914586	5.101727	0.0228	8.9	0.17	0.44	205 ± 2	102 ± 5	0.8 ± 0.7	4.04 ± 0.02	-4.3 ± 0.4	35.5 ± 0.7	4.3 ± 0.3	SF-AGN
11754-3701*	129.710888	1.405020	0.0290	9.3	1.16	0.51	231 ± 6	156 ± 19	5.2 ± 0.5	4.50 ± 0.01	-3.54 ± 0.04	36.6 ± 0.5	6.1 ± 0.1	SF-AGN
11826-12702	188.522918	36.841747	0.0402	9.7	0.74	0.34	227 ± 6	132 ± 8	4.8 ± 0.5	4.16 ± 0.01	-4.24 ± 0.04	35.65 ± 0.06	4.78 ± 0.04	SF-AGN
12487-3704	139.326370	29.727896	0.0341	9.6	0.16	1.00	261 ± 13	141 ± 11	1.9 ± 0.4	4.65 ± 0.02	-3.37 ± 0.05	36.61 ± 0.07	5.76 ± 0.06	AGN
7992-6102*	253.889080	63.242118	0.0225	9.6	1.63	0.30	226 ± 19	120 ± 15	2.1 ± 0.3	4.19 ± 0.01	-3.8 ± 0.1	36.3 ± 1.4	5.77 ± 0.09	SF-AGN
8655-6101*	358.094460	-0.628760	0.0226	9.6	0.09	0.62	257 ± 18	161 ± 33	1.5 ± 0.2	3.91 ± 0.02	-3.71 ± 0.08	36.4 ± 0.3	5.8 ± 0.1	AGN
8657-6104*	10.417361	0.208729	0.0175	8.7	0.12	0.24	213 ± 4	96 ± 6	0.4 ± 0.2	3.19 ± 0.04	-4.43 ± 0.08	35.4 ± 0.1	4.37 ± 0.08	SF-AGN
8982-3703	203.190090	26.580376	0.0470	9.4	0.92	1.00	566 ± 5	441 ± 5	2.2 ± 0.5	5.85 ± 0.01	-1.28 ± 0.01	39.46 ± 0.01	8.61 ± 0.01	AGN ^{††}
9889-1902	234.858582	24.943586	0.0228	9.7	1.11	0.78	333 ± 7	206 ± 10	2.5 ± 0.5	5.55 ± 0.01	-1.77 ± 0.01	38.75 ± 0.01	8.14 ± 0.01	AGN ^{††}

Column designation: (1) MaNGA plateifu; (2,3) RA, DEC coordinates of the optical center of the galaxy or IFU center; (4) galaxy redshift; (5) galaxy stellar mass; (6) star formation rate derived from $H\alpha$; (7) AGN fraction (8) median value of the W_{80} velocity; (9) median value of the velocity of the outflow; (10) radius of the outflow; (11) ionized gas mass of the outflow; (12) ionized gas mass outflow rate; (13) ionized gas kinetic energy outflow rate; (14) ionized gas momentum outflow rate; (15) MaNGA BPT classification. * Galaxies without fully extended outflow. [†] MIR AGN, ^{††} radio AGN (see Mezcuca & Domínguez Sánchez 2024).

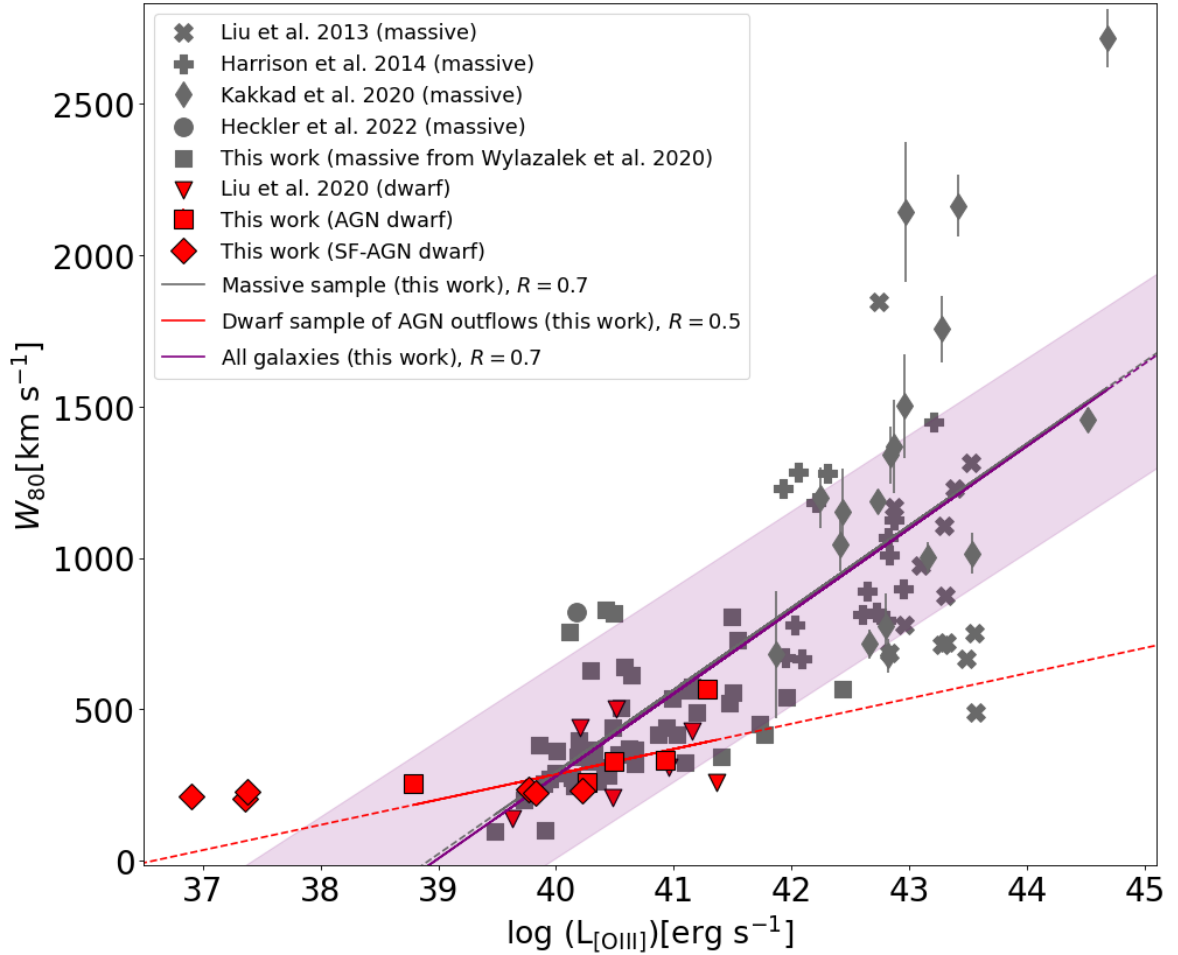


Fig. 6: W_{80} velocity vs $L_{[\text{OIII}]}$ for the MaNGA sample of 11 dwarf galaxies with AGN outflow candidates (red squares for AGN galaxies, red diamonds for SF-AGN galaxies), the AGN dwarf galaxy sample of Liu et al. (2020) (red triangles), the $z < 2$ type-2 AGN quasars of Harrison et al. (2014) (grey pluses), the radio-quiet quasars of Liu et al. (2013) (grey crosses), the $z \sim 2$ type-1 massive AGN of Kakkad et al. (2020) (grey diamonds), the massive LLAGN of Heckler et al. (2022) (grey circle) and the MaNGA sample of low-intermediate luminosity massive galaxies of Wylazalek et al. (2020) (grey squares). The solid lines are regression fits to the massive sample (grey), the dwarf sample of AGN outflows, which includes the seven MaNGA dwarf galaxies with AGN outflows and those from Liu et al. (2020) (red), and the combination of all the massive galaxies and the dwarf sample of AGN outflows (purple) being the shaded area the 1σ error of the regression line.

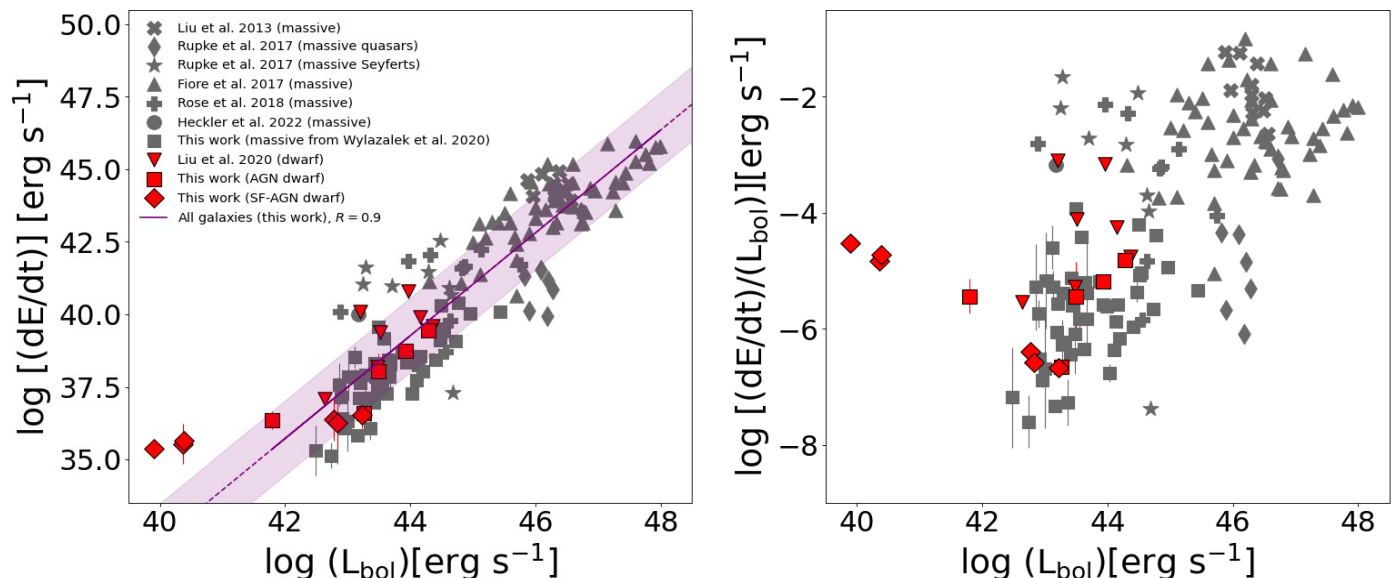


Fig. 7: Ionized outflow kinetic energy rate vs AGN bolometric luminosity (left) and ratio of the kinetic energy outflow rate to the AGN bolometric luminosity (right) for the MaNGA sample of dwarf galaxies with AGN outflow candidates (red squares for AGN galaxies, red diamonds for SF-AGN galaxies), the AGN dwarf galaxy sample of Liu et al. (2020) (red triangles), the radio-quiet quasars of Liu et al. (2013) (grey crosses), the type 1 quasars of Rupke et al. (2017) (grey diamonds), the ULIRGs of Rose et al. (2018) (grey pluses), the MaNGA sample of low-intermediate luminosity massive galaxies of Wylezalek et al. (2020) (grey squares), and the massive LLAGN of Heckler et al. (2022) (grey circle). The purple solid line is a regression fit considering all the massive galaxies, the seven MaNGA dwarf galaxies with AGN outflows, and those from Liu et al. (2020). The shaded area corresponds to the 1σ error of the regression line.

the Low Luminosity Active Galactic Nuclei (LLAGN) with AGN outflows studied in Heckler et al. (2022), the $z \sim 0.5$ radio-quiet quasars with AGN outflows studied in Liu et al. (2013), the $z < 0.2$ massive type-2 AGN quasars with AGN outflows studied in Harrison et al. (2014), and the $z \sim 2$ massive type-1 AGN with AGN outflows studied in Kakkad et al. (2020). The typical velocity of the AGN outflow candidates in dwarf galaxies seems to be $< 500 \text{ km s}^{-1}$, while those of massive galaxies often surpasses the 500 km s^{-1} and, in some cases, even the 2000 km s^{-1} (e.g. Kakkad et al. 2020). However, 29 massive but low-intermediate luminosity galaxies from Wylezalek et al. (2020) whose W_{80} velocities have been recalculated in this paper present velocities $W_{80} < 500 \text{ km s}^{-1}$. We perform a linear regression to the sample of massive galaxies (Liu et al. 2013; Harrison et al. 2014; Wylezalek et al. 2020; Kakkad et al. 2020), henceforth ‘massive sample’. We also fit a linear regression including just the seven MaNGA dwarf galaxies with AGN outflows in addition to those studied in Liu et al. (2020) (henceforth ‘dwarf sample’), and another one for all the galaxies, massives and dwarves, but excluding the four MaNGA dwarf galaxies with uncertain outflows. Comparing the results of all the regression lines (see Table 4), the one that includes all the galaxies and the one for the massive sample have similar values for both the slope and the correlation coefficient, being the regression lines almost overlapped. They have higher correlation coefficient than the one for the dwarf sample. These results could suggest that the AGN outflows in dwarf galaxies can be produced by the same mechanisms as those in massive galaxies, being the dwarves a scaled-down version of the massive ones (see also Liu et al. 2020). However, the slope of the fit for the dwarf sample is a 69% lower than the one for the all galaxies sample and for the massive sample (see Table 4). This may indicate that the W_{80}

velocity for the dwarf sample does not follow the same trend as all the galaxies.

3.7.1. Kinetic energy rate and L_{bol}

The kinetic energy outflow rate is a parameter used as a measure of how powerful the outflow is. The values of kinetic energy rate normalized by L_{bol} (i.e. outflow efficiency) are shown in Table 3. Fig. 7 shows, following Liu et al. (2020), dE/dt vs L_{bol} (left) and $(dE/dt)/L_{\text{bol}}$ vs L_{bol} (right) for the same literature we use in W_{80} velocity vs $[OIII]$ luminosity in the case of our MaNGA sample of 11 dwarf galaxies with AGN outflow candidates, Liu et al. (2020), Wylezalek et al. (2020) (whose kinetic energy rates are derived in this paper), Heckler et al. (2022), and Liu et al. (2013) in addition to the type 1 quasars with AGN outflows of Rupke et al. (2017), the different AGN at different redshifts ($z=0.1-3$) of Fiore et al. 2017, and the Ultraluminous Infrared Galaxies (ULIRGs) with AGN outflows of Rose et al. 2018. The bolometric luminosity is calculated from the $L_{[OIII]}$ using a bolometric correction factor of 1000 (Moran et al. 2014) except for those galaxies in Rupke et al. (2017) and Fiore et al. (2017) whose $L_{[OIII]}$ is not reported and the bolometric luminosity is calculated either from $L_{\text{bol}} = 1.15 \times L_{\text{IR}}$, being L_{IR} the infrared luminosity, and from fitting optical-ultraviolet spectral energy distribution. The kinetic energy rate of the 11 MaNGA dwarf galaxies with AGN outflows candidates is four to six orders of magnitude lower than their bolometric luminosity. This suggests that it would be difficult for the outflow to have a significant impact in the galaxy as a source of feedback (Wang et al. 2024), although there may be additional outflow mass hidden in other phases (Belli et al. 2023) such as warm and cold molecular gas phases. This result is consistent with that regarding the mass-loading factor, where we find that the outflows are unlikely

MaNGA plateifu (1)	$\log(L_{\text{OIII}})$ (erg s^{-1}) (2)	$\log(L_{\text{bol}})$ (erg s^{-1}) (3)	$\log[(dE/dt)/(L_{\text{bol}})]$ (4)
10223-3702	40.5	43.5	-5.4
10226-1901	39.8	42.8	-6.4
11022-12702	37.4	40.4	-4.8
11754-3701	40.2	43.2	-6.7
11826-12702	37.4	40.4	-4.7
12487-3704	40.3	43.3	-6.6
7992-6102	39.8	42.8	-6.6
8655-6101	38.8	41.8	-5.4
8657-6104	36.9	39.9	-4.5
8982-3703	41.3	44.3	-4.8
9889-1902	40.9	43.9	-5.2

Table 3: **Column designation:** (1) MaNGA plateifu; (2) [OIII] luminosity; (3) AGN bolometric luminosity derived as $L_{\text{bol}} = 1000 \times L_{\text{[OIII]}}$ (Moran et al. 2014); (4) Ratio between the kinetic outflow rate of the outflow and the bolometric luminosity of the AGN

Sample	Slope	R	p-value
Massive sample	271 ± 26	0.73	3.9×10^{-17}
Dwarf sample	83 ± 42	0.49	0.07
All galaxies sample	272 ± 22	0.75	2.9×10^{-21}

Table 4: Regression lines of the W_{80} vs $L_{\text{[OIII]}}$ correlation.

to quench the SF (see Sect. 3.5). Additionally, a linear regression is performed between $\log(dE/dt)$ vs $\log(L_{\text{bol}})$, including all the galaxies except for the four MaNGA dwarf galaxies with uncertain outflows. The correlation coefficient is $R = 0.9$ indicating that both dwarf and massive galaxies behave similar. In addition to this, a Mann-Whitney U rank test is performed on two independent samples (massives and dwarves) returning ap-value > 0.3 in both cases. Consequently, the null hypothesis that the $(dE/dt)/L_{\text{bol}}$ of dwarf and massive galaxies is drawn from the same distribution cannot be rejected. These results may indicate that AGN outflows in dwarf galaxies behave in a similar way than that of massive galaxies, in agreement with the linear correlation when comparing the outflow velocity against the [OIII] luminosity in the ‘All galaxies sample’ of Fig. 6. However, the outflow efficiency does not only depend on the AGN luminosity, but also on other factors such as the orientation of the outflow with respect to the galaxy disk (Harrison & Ramos Almeida 2024). Thus, a more robust study should be done, but is beyond the scope of the current work.

4. Conclusions

Dwarf galaxies are the most abundant type of galaxies and the building blocks of the more massive ones. Although they were commonly assumed to be regulated by SNe feedback, in the last decades thousands of AGN have been found in dwarf galaxies. Furthermore, recent studies have shown evidence for the presence of AGN outflows and feedback that may have an impact in the growth of the galaxy. In this paper, the presence of AGN outflows in a sample of 2292 dwarf galaxies, characterized

by strong AGN signatures (Mezcua & Domínguez Sánchez 2024), has been studied. These galaxies are drawn from the MaNGA survey and thus IFU data is available. The stacked spectrum of all those spaxels classified as AGN are fitted using the GELATO python code. For those galaxies in which a broad component in the [OIII] $\lambda 5007\text{\AA}$ emission line is fitted, GELATO is run again through all the AGN spaxels in order to spatially resolve this outflowing component and study the kinematic and energetic properties. We find 11 new dwarf galaxies with AGN outflow candidates. The main results of this study are:

- For eight out of the 11 MaNGA AGN dwarf galaxies there is a misalignment between the gas and the stellar kinematics that may indicate the presence of potential outflows.
- The outflow velocity W_{80} of the 11 MaNGA AGN dwarf galaxies ranges from 205 to 566 km s^{-1} which is lower than the typical values of massive galaxies, which often surpasses the 500 km s^{-1} , reaching values above 1000 km s^{-1} .
- For seven out of the 11 MaNGA AGN dwarf galaxies, the AGN is the most likely mechanism to drive these outflows based on the AGN fraction, the W_{80} velocity and the L_{bol} (see Sect. 3.4). For the remaining four galaxies, both SNe and AGN are possible candidates for driving these outflows.
- The AGN outflow velocity, W_{80} , in one out of the 11 MaNGA dwarf galaxies with outflows is higher than the dark matter halo escape velocity. For that galaxy, an enrichment of the circumgalactic medium is expected.
- We find a correlation between outflow velocity W_{80} and $L_{\text{[OIII]}}$ that extends all the way from massive to dwarf galaxies with AGN outflows. This may indicate that AGN outflows in dwarf galaxies can be a scaled-down version of massive galaxies. However, the slope of the regression line of the dwarf sample is lower than the one including all galaxies, suggesting that the correlation might not be followed by the AGN outflows in dwarf galaxies.
- The kinetic energy outflow rate for the sample of 11 MaNGA dwarf galaxies with AGN outflow candidates ranges from 10^{35} to 10^{39} erg s^{-1} . The relation between kinetic energy rate and the bolometric luminosity seems to follow a linear relationship through all the mass regime. However, we find that three out of the 11 MaNGA dwarf galaxies with AGN outflows signatures do not follow this linear relationship, although the origin of the outflow for these galaxies is uncertain. Also, we find that massive and dwarf galaxies are drawn from the same distribution when comparing the outflow efficiency against the bolometric luminosity.

In this work we give arguments for AGN outflows in dwarf galaxies behaving similar than those in massive galaxies. However, we find three galaxies that do not follow the linear trends showed in this work, although the driven mechanism that causes the outflow in these three galaxies is not well known. Therefore, the necessity of new detections of AGN outflows in dwarf galaxies is crucial in order to have a better understanding of them, their impact and their role in terms of galaxy evolution.

In a future work, we plan to study the stellar population properties and examine the effects of SNe in these 11 dwarf galaxies with AGN outflow candidates to further understand the feedback processes and their impact on galaxy evolution.

Acknowledgements. The authors thank the anonymous referee for insightful comments. The authors acknowledge the feedback received from Rogemar Riffel and Rogério Riffel from the Universidade Federal de Santa Maria and from the Universidade Federal do Rio Grande do Sul respectively and from all the colleagues of the AGN and galaxy evolution group of the Institut de Space Sciences of Barcelona. The authors also acknowledge the help provided by Raphael Hviding from the Arizona University and the Max-Planck Institute for Astronomy. VRM acknowledges support from the Spanish Ministry of Science, Innovation and Universities through the project PRE2022-104649. MM and AE acknowledge support from the Spanish Ministry of Science and Innovation through the project PID2021-124243NB-C22. This work was partially supported by the program Unidad de Excelencia María de Maeztu CEX2020-001058-M. HDS acknowledges the financial support from the Spanish Ministry of Science and Innovation and the European Union - NextGenerationEU through the Recovery and Resilience Facility project ICTS MRR-2021-03-CEFCA and financial support provided by the Governments of Spain and Aragón through their general budgets and the Fondo de Inversiones de Teruel. HDS acknowledges financial support by RyC2022-030469-I grant, funded by MCIN/AEI/10.13039/501100011033 and FSE+. AA acknowledges funding from the MICINN (Spain) through the Juan de la Cierva-Formación program under contract FJC2020-046224-I and support by the European Union grant WIDERA ExGal-Twin, GA 101158446. F.M-S. acknowledges support from NASA through ADAP award 80NSSC19K1096. M.S. acknowledges support by the State Research Agency of the Spanish Ministry of Science and Innovation under the grants 'Galaxy Evolution with Artificial Intelligence' (PGC2018-100852-A-I00) and 'BASALT' (PID2021-126838NB-I00) and the Polish National Agency for Academic Exchange (Bekker grant BPN/BEK/2021/1/00298/DEC/1). This work was partially supported by the European Union's Horizon 2020 Research and Innovation program under the Maria Skłodowska-Curie grant agreement (No. 754510).

References

- Akaike, H. 1974, *IEEE transactions on automatic control*, 19, 716
- Aravindan, A., Liu, W., Canalizo, G., et al. 2023, *The Astrophysical Journal*, 950, 33
- Arce, H. G., Shepherd, D., Gueth, F., et al. 2006, *arXiv preprint astro-ph/0603071*
- Arjona-Galvez, E., Di Cintio, A., & Grand, R. J. 2024, *Astronomy & Astrophysics*, 690, A286
- Baldassare, V. F., Reines, A. E., Gallo, E., & Greene, J. E. 2015, *The Astrophysical Journal Letters*, 809, L14
- Baldwin, J. A., Phillips, M. M., & Terlevich, R. 1981, *Publications of the Astronomical Society of the Pacific*, 93, 5
- Bally, J. 2008, in *Massive Star Formation: Observations Confront Theory*, Vol. 387, 158
- Barai, P. & Dal Pino, E. M. d. G. 2018, *Proceedings of the International Astronomical Union*, 14, 154
- Belfiore, F., Westfall, K. B., Schaefer, A., et al. 2019, *The Astronomical Journal*, 158, 160
- Belli, S., Park, M., Davies, R. L., et al. 2023, *arXiv preprint arXiv:2308.05795*
- Bellovary, J. M., Cleary, C. E., Munshi, F., et al. 2019, *Monthly Notices of the Royal Astronomical Society*, 482, 2913
- Bianchi, L., Herald, J., Efremova, B., et al. 2011, *Astrophysics and Space Science*, 335, 161
- Bianchi, L., Shiao, B., & Thilker, D. 2017, *The Astrophysical Journal Supplement Series*, 230, 24
- Birchall, K. L., Watson, M., & Aird, J. 2020, *Monthly Notices of the Royal Astronomical Society*, 492, 2268
- Bohn, T., Canalizo, G., Veilleux, S., & Liu, W. 2021, *The Astrophysical Journal*, 911, 70
- Boquien, M., Burgarella, D., Roehlly, Y., et al. 2019, *Astronomy & Astrophysics*, 622, A103
- Bower, R. G., Benson, A., Malbon, R., et al. 2006, *Monthly Notices of the Royal Astronomical Society*, 370, 645
- Bruzual, G. & Charlot, S. 2003, *Monthly Notices of the Royal Astronomical Society*, 344, 1000
- Bundy, K., Bershad, M. A., Law, D. R., et al. 2015, *The Astrophysical Journal*, 798
- Bykov, S., Gilfanov, M., & Sunyaev, R. 2024, *Monthly Notices of the Royal Astronomical Society*, 527, 1962
- Calzetti, D., Armus, L., Bohlin, R. C., et al. 2000, *The Astrophysical Journal*, 533, 682
- Capelo, P. R., Feruglio, C., Hickox, R. C., & Tombesi, F. 2024, in *Handbook of X-ray and Gamma-ray Astrophysics (Springer)*, 4567–4616
- Carniani, S., Venturi, G., Parlanti, E., et al. 2024, *Astronomy & Astrophysics*, 685, A99
- Casanueva, C. I., Lagos, C. d. P., Padilla, N. D., & Davison, T. A. 2022, *Monthly Notices of the Royal Astronomical Society*, 514, 2031
- Chabrier, G. 2003, *The Astrophysical Journal*, 586, L133
- Chilingarian, I. V., Katkov, I. Y., Zolotukhin, I. Y., et al. 2018, *The Astrophysical Journal*, 863, 1
- Churchwell, E. 1997, *The Astrophysical Journal*, 479, L59
- Cid Fernandes, R. C., Stasińska, G., Schlickmann, M., et al. 2010, *Monthly Notices of the Royal Astronomical Society*, 403, 1036
- Clavijo-Bohórquez, W. E., de Gouveia Dal Pino, E. M., & Melioli, C. 2024, *Monthly Notices of the Royal Astronomical Society*, 535, 1696
- Comerford, J. M. & Greene, J. E. 2014, *The Astrophysical Journal*, 789, 112
- Commerçon, B., González, M., Mignon-Risse, R., Hennebelle, P., & Vaytet, N. 2022, *Astronomy & Astrophysics*, 658, A52
- Croton, D. J., Springel, V., White, S. D., et al. 2006, *Monthly Notices of the Royal Astronomical Society*, 365, 11
- Cutri, R., Skrutskie, M., Van Dyk, S., et al. 2003, *VizieR Online Data Catalog*, II
- Cutri, R., Skrutskie, M., van Dyk, S., et al. 2012, *VizieR Online Data Catalog*, II
- Cutri, R. e., Wright, E., Conrow, T., et al. 2021, *VizieR Online Data Catalog*, II
- da Silva, P., Steiner, J. E., & Menezes, R. 2017, *Monthly Notices of the Royal Astronomical Society*, 470, 3850
- Doi, M., Tanaka, M., Fukugita, M., et al. 2010, *The Astronomical Journal*, 139, 1628
- Draine, B., Aniano, G., Krause, O., et al. 2013, *The Astrophysical Journal*, 780, 172
- Falceta-Gonçalves, D., Caproni, A., Abraham, Z., Teixeira, D., & Dal Pino, E. d. G. 2010, *The Astrophysical Journal Letters*, 713, L74
- Filippenko, A. V. & Sargent, W. L. 1989, *The Astrophysical Journal*, 342, L11
- Fiore, F., Feruglio, C., Shankar, F., et al. 2017, *Astronomy & Astrophysics*, 601, A143
- Fritz, J., Franceschini, A., & Hatziminaoglou, E. 2006, *Monthly Notices of the Royal Astronomical Society*, 366, 767
- Fukugita, M., Shimasaku, K., Ichikawa, T., Gunn, J., et al. 1996, *The Sloan digital sky survey photometric system*, Tech. rep., SCAN-9601313
- Gatto, A., Walch, S., Naab, T., et al. 2017, *Monthly Notices of the Royal Astronomical Society*, 466, 1903
- Greene, J. E. & Ho, L. C. 2007, *The Astrophysical Journal*, 670, 92

- Hao, L., Strauss, M. A., Tremonti, C. A., et al. 2005, *The Astronomical Journal*, 129, 1783
- Harrison, C., Alexander, D., Mullaney, J., & Swinbank, A. 2014, *Monthly Notices of the Royal Astronomical Society*, 441, 3306
- Harrison, C. M. & Ramos Almeida, C. 2024, *Galaxies*, 12, 17
- Hasinger, G. 2008, *Astronomy & Astrophysics*, 490, 905
- Heckler, K. F., Ricci, T. V., & Riffel, R. A. 2022, *Monthly Notices of the Royal Astronomical Society*, 517, 5959
- Hickox, R. C. & Alexander, D. M. 2018, *Annual Review of Astronomy and Astrophysics*, 56, 625
- Holt, J., Tadhunter, C., & Morganti, R. 2008, *Monthly Notices of the Royal Astronomical Society*, 387, 639
- Hopkins, A. M., Miller, C., Nichol, R., et al. 2003, *The Astrophysical Journal*, 599, 971
- Hviding, R. E., Hainline, K. N., Rieke, M., et al. 2022, *The Astronomical Journal*, 163, 224
- Inoue, A. K. 2011, *Monthly Notices of the Royal Astronomical Society*, 415, 2920
- Jarrett, T., Cohen, M., Masci, F., et al. 2011, *The Astrophysical Journal*, 735, 112
- Johnston, V. D., Medling, A. M., Groves, B., et al. 2023, *The Astrophysical Journal*, 954, 77
- Kakkad, D., Mainieri, V., Vietri, G., et al. 2020, *Astronomy & Astrophysics*, 642, A147
- Kauffmann, G., Heckman, T. M., Tremonti, C., et al. 2003, *Monthly Notices of the Royal Astronomical Society*, 346, 1055
- Kennicutt Jr, R. C. 1998, *Annual Review of Astronomy and Astrophysics*, 36, 189
- Kennicutt Jr, R. C. & Evans, N. J. 2012, *Annual Review of Astronomy and Astrophysics*, 50, 531
- Kewley, L. J., Dopita, M., Sutherland, R., Heisler, C., & Trevena, J. 2001, *The Astrophysical Journal*, 556, 121
- Kewley, L. J., Geller, M. J., & Jansen, R. A. 2004, *The Astronomical Journal*, 127, 2002
- Kewley, L. J., Groves, B., Kauffmann, G., & Heckman, T. 2006, *Monthly Notices of the Royal Astronomical Society*, 372, 961
- Kollatschny, W. & Zetzl, M. 2013, *Astronomy & Astrophysics*, 549, A100
- Kormendy, J. & Ho, L. C. 2013, *Annual Review of Astronomy and Astrophysics*, 51, 511
- Koudmani, S., Sijacki, D., & Smith, M. C. 2022, *Monthly Notices of the Royal Astronomical Society*, 516, 2112
- Krajinovic, D., Cappellari, M., De Zeeuw, P. T., & Copin, Y. 2006, *Monthly Notices of the Royal Astronomical Society*, 366, 787
- Leung, G. C., Coil, A. L., Aird, J., et al. 2019, *The Astrophysical Journal*, 886, 11
- Liu, G., Zakamska, N. L., Greene, J. E., Nesvadba, N. P., & Liu, X. 2013, *Monthly Notices of the Royal Astronomical Society*, 436, 2576
- Liu, W., Veilleux, S., Canalizo, G., et al. 2020, *The Astrophysical Journal*, 905, 166
- Liu, W., Veilleux, S., Canalizo, G., et al. 2024, *The Astrophysical Journal*, 965, 152
- Łokas, E. L. & Mamon, G. A. 2001, *Monthly Notices of the Royal Astronomical Society*, 321, 155
- Manzano-King, C. M., Canalizo, G., & Sales, L. V. 2019, *The Astrophysical Journal*, 884, 54
- Maraston, C., Pforr, J., Henriques, B. M., et al. 2013, *Monthly Notices of the Royal Astronomical Society*, 435, 2764
- Marleau, F. R., Clancy, D., Habas, R., & Bianconi, M. 2017, *Astronomy & Astrophysics*, 602, A28
- Martín-Navarro, I. & Mezcuca, M. 2018, *The Astrophysical Journal Letters*, 855, L20
- Mezcuca, M., Civano, F., Fabbiano, G., Miyaji, T., & Marchesi, S. 2016, *The Astrophysical Journal*, 817, 20
- Mezcuca, M., Civano, F., Marchesi, S., et al. 2018, *Monthly Notices of the Royal Astronomical Society*, 478, 2576
- Mezcuca, M. & Domínguez Sánchez, H. D. 2020, *The Astrophysical Journal Letters*, 898, L30
- Mezcuca, M. & Domínguez Sánchez, H. D. 2024, *Monthly Notices of the Royal Astronomical Society*, stae292
- Mezcuca, M., Pacucci, F., Suh, H., Siudek, M., & Natarajan, P. 2024, *The Astrophysical Journal Letters*, 966, L30
- Mezcuca, M., Siudek, M., Suh, H., et al. 2023, *The Astrophysical Journal Letters*, 943, L5
- Mezcuca, M., Suh, H., & Civano, F. 2019, *Monthly Notices of the Royal Astronomical Society*, 488, 685
- Moran, E. C., Shahinyan, K., Sugarman, H. R., Vélez, D. O., & Eracleous, M. 2014, *The Astronomical Journal*, 148, 136
- Moster, B. P., Naab, T., & White, S. D. 2013, *Monthly Notices of the Royal Astronomical Society*, 428, 3121
- Moster, B. P., Somerville, R. S., Maubetsch, C., et al. 2010, *The Astrophysical Journal*, 710, 903
- Mullaney, J., Alexander, D., Fine, S., et al. 2013, *Monthly Notices of the Royal Astronomical Society*, 433, 622
- Navarro, J. F., Frenk, C. S., & White, S. D. 1997, *The Astrophysical Journal*, 490, 493
- Osborne, C., Salim, S., Boquien, M., Dickinson, M., & Arnouts, S. 2023, *The Astrophysical Journal Supplement Series*, 268, 26
- Osterbrock, D. E. & Ferland, G. J. 2006, *Astrophysics of gaseous nebulae and active galactic nuclei*, 2nd
- Penny, S. J., Masters, K. L., Smethurst, R., et al. 2018, *Monthly Notices of the Royal Astronomical Society*, 476, 979
- Pucha, R., Juneau, S., Dey, A., et al. 2024, *arXiv preprint arXiv:2411.00091*
- Raimundo, S. I., Malkan, M., & Vestergaard, M. 2023, *Nature Astronomy*, 7, 463
- Reines, A. E., Condon, J. J., Darling, J., & Greene, J. E. 2020, *The Astrophysical Journal*, 888, 36
- Reines, A. E., Greene, J. E., & Geha, M. 2013, *The Astrophysical Journal*, 775, 116
- Ricci, T., Steiner, J. E., & Menezes, R. 2014, *Monthly Notices of the Royal Astronomical Society*, 440, 2419
- Ristea, A., Cortese, L., Fraser-McKelvie, A., et al. 2022, *Monthly Notices of the Royal Astronomical Society*, 517, 2677
- Romano, M., Nanni, A., Donevski, D., et al. 2023, *Astronomy & Astrophysics*, 677, A44
- Rose, M., Tadhunter, C., Ramos Almeida, C., et al. 2018, *Monthly Notices of the Royal Astronomical Society*, 474, 128
- Rosen, A. L. 2022, *The Astrophysical Journal*, 941, 202
- Rupke, D. S., Gültekin, K., & Veilleux, S. 2017, *The Astrophysical Journal*, 850, 40
- Salehirad, S., Reines, A. E., & Molina, M. 2022, *The Astrophysical Journal*, 937, 7
- Salehirad, S., Reines, A. E., & Molina, M. 2024, *arXiv preprint arXiv:2412.00880*
- Sanders, R. L., Shapley, A. E., Kriek, M., et al. 2015, *The Astrophysical Journal*, 816, 23
- Sarzi, M., Falcón-Barroso, J., Davies, R. L., et al. 2006, *Monthly Notices of the Royal Astronomical Society*, 366, 1151
- Sau, S., Chattopadhyay, T., & Ray, P. 2023, *New Astronomy*, 100, 101992
- Siudek, M., Pucha, R., Mezcuca, M., et al. 2024, *Astronomy & Astrophysics*, 691, A308

- Skrutskie, M., Cutri, R., Stiening, R., et al. 2006, *The Astronomical Journal*, 131, 1163
- Smethurst, R. J., Simmons, B. D., Coil, A., et al. 2021, *Monthly Notices of the Royal Astronomical Society*, 507, 3985
- Stern, D., Assef, R. J., Benford, D. J., et al. 2012, *The Astrophysical Journal*, 753, 30
- Tanner, R. & Weaver, K. A. 2022, *The Astronomical Journal*, 163, 134
- Trebitsch, M., Volonteri, M., Dubois, Y., & Madau, P. 2018, *Monthly Notices of the Royal Astronomical Society*, 478, 5607
- Vazdekis, A., Koleva, M., Ricciardelli, E., Röck, B., & Falcón-Barroso, J. 2016, *Monthly Notices of the Royal Astronomical Society*, 463, 3409
- Veilleux, S., Cecil, G., & Bland-Hawthorn, J. 2005, *Annu. Rev. Astron. Astrophys.*, 43, 769
- Vietri, G., Garilli, B., Polletta, M., et al. 2022, *Astronomy & Astrophysics*, 659, A129
- Wang, B., de Graaff, A., Davies, R. L., et al. 2024, arXiv preprint arXiv:2403.02304
- Westfall, K. B., Cappellari, M., Bershady, M. A., et al. 2019, *The Astronomical Journal*, 158, 231
- Winiarska, M. W., Raimundo, S. I., Davis, T. A., et al. 2025, *Monthly Notices of the Royal Astronomical Society*, staf295
- Wright, E. L., Eisenhardt, P. R., Mainzer, A. K., et al. 2010, *The Astronomical Journal*, 140, 1868
- Wylezalek, D., Flores, A. M., Zakamska, N. L., Greene, J. E., & Riffel, R. A. 2020, *Monthly Notices of the Royal Astronomical Society*, 492, 4680
- Zheng, Z., Shi, Y., Bian, F., et al. 2023, *Monthly Notices of the Royal Astronomical Society*, 523, 3274
- Zhuang, M.-Y. & Ho, L. C. 2023, *Nature Astronomy*, 7, 1376
- Zinchenko, I. 2023, *Astronomy & Astrophysics*, 674, L7

Appendix A: Effects on SNR threshold selection

Mezcua & Domínguez Sánchez (2024) perform a spaxel classification only considering spaxels with $\text{SNR} \geq 3$ in the BPT emission lines ($\text{H}\alpha$, $\text{H}\beta$, $[\text{NII}]\lambda 6583$, $[\text{SII}]\lambda 6718$, $[\text{SII}]\lambda 6732$, $[\text{OIII}]\lambda 5007$, $[\text{OI}]\lambda 6300$). This is something commonly adopted in BPT studies (e.g. Reines et al. 2013 for SDSS; Wylezalek et al. 2020 for MaNGA; Salehirad et al. 2022 for GAMA; Johnston et al. 2023 for SAMI). However, in our analysis we consider only spaxels with $\text{SNR} \geq 10$ to ensure reliable spectral fittings. In Fig. A.1, the spatial distribution of the SNR is shown together with the extension of the outflows of Figs. 2 and 3 but considering a $\text{SNR} > 3$ in the outflow spaxels. No sources with AGN outflows are missed when using $\text{SNR} \geq 10$ rather than $\text{SNR} \geq 3$.

Appendix B: Outflow, $[\text{OIII}]\lambda 5007$ and stellar velocity maps

Figs. B.1-B.9 show the outflow, $[\text{OIII}]\lambda 5007$ and stellar velocity maps of the remaining 9 dwarf galaxies with AGN outflow signatures, as in Figs. 2 and 3.

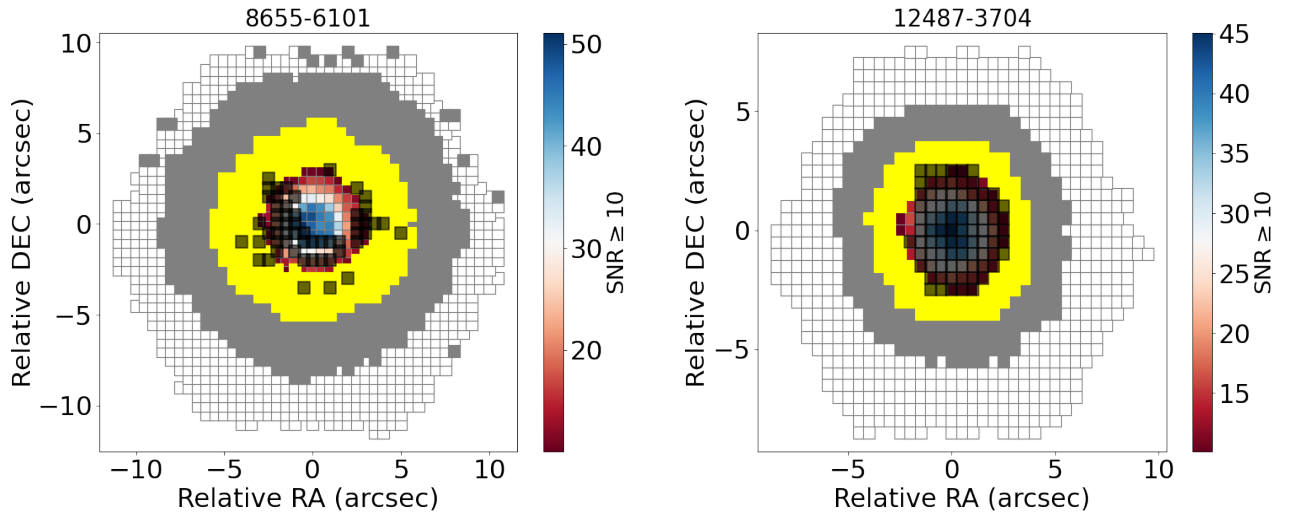


Fig. A.1: Spatial distribution of the SNR for the same two examples as in Figs. 2 and 3. The colourbar is set for those spaxels with $\text{SNR} \geq 10$. Those spaxels with $3 \leq \text{SNR} < 10$ are shown in yellow to highlight the number of spaxels that would be missed when applying a threshold of $\text{SNR} \geq 10$ rather than $\text{SNR} \geq 3$ to ensure the goodness of the fit. The shaded dark spaxels represent the extension of the AGN outflow in each galaxy.

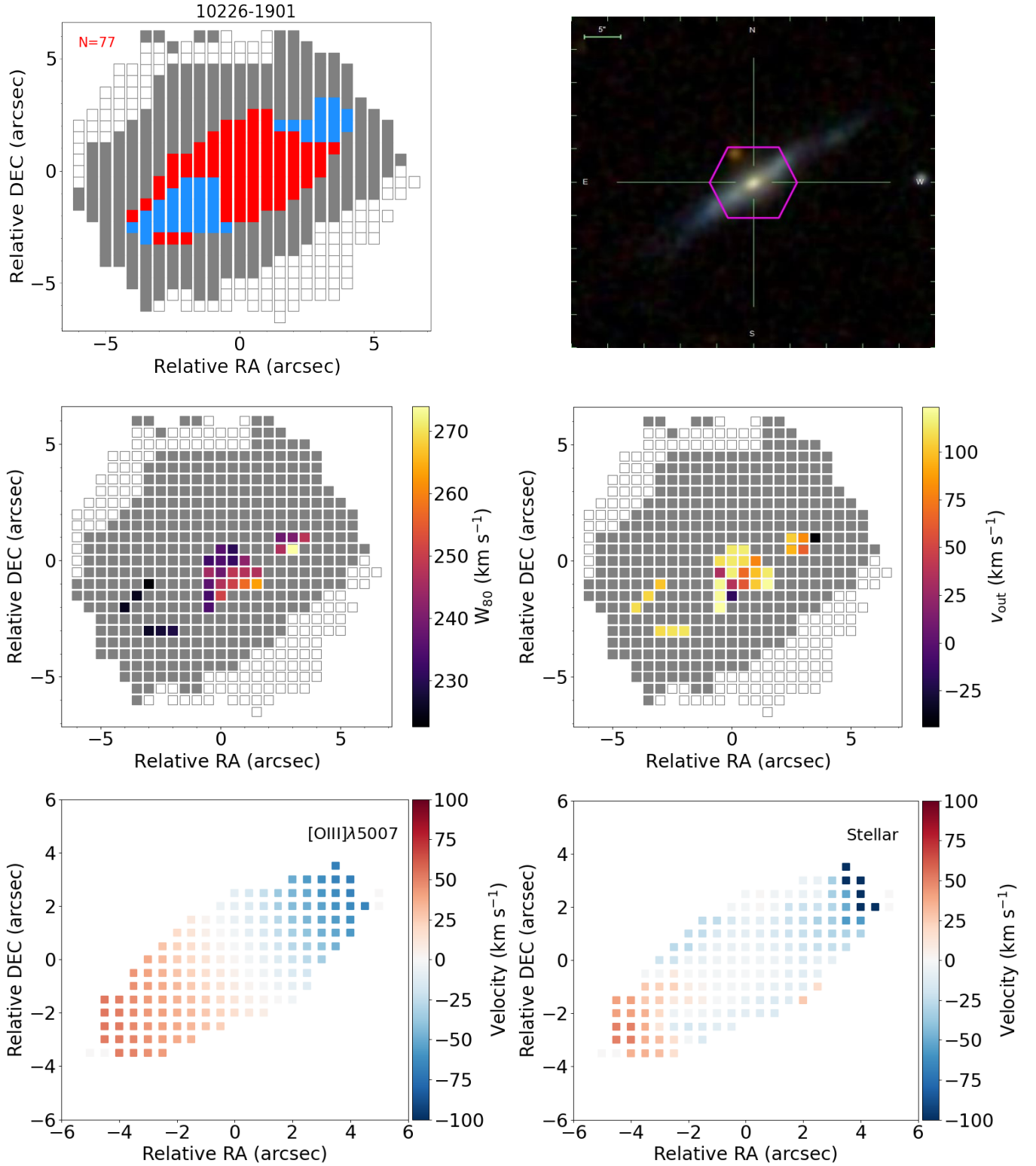


Fig. B.1: Same caption as in Fig. 2 for the dwarf galaxy 10226-1902.

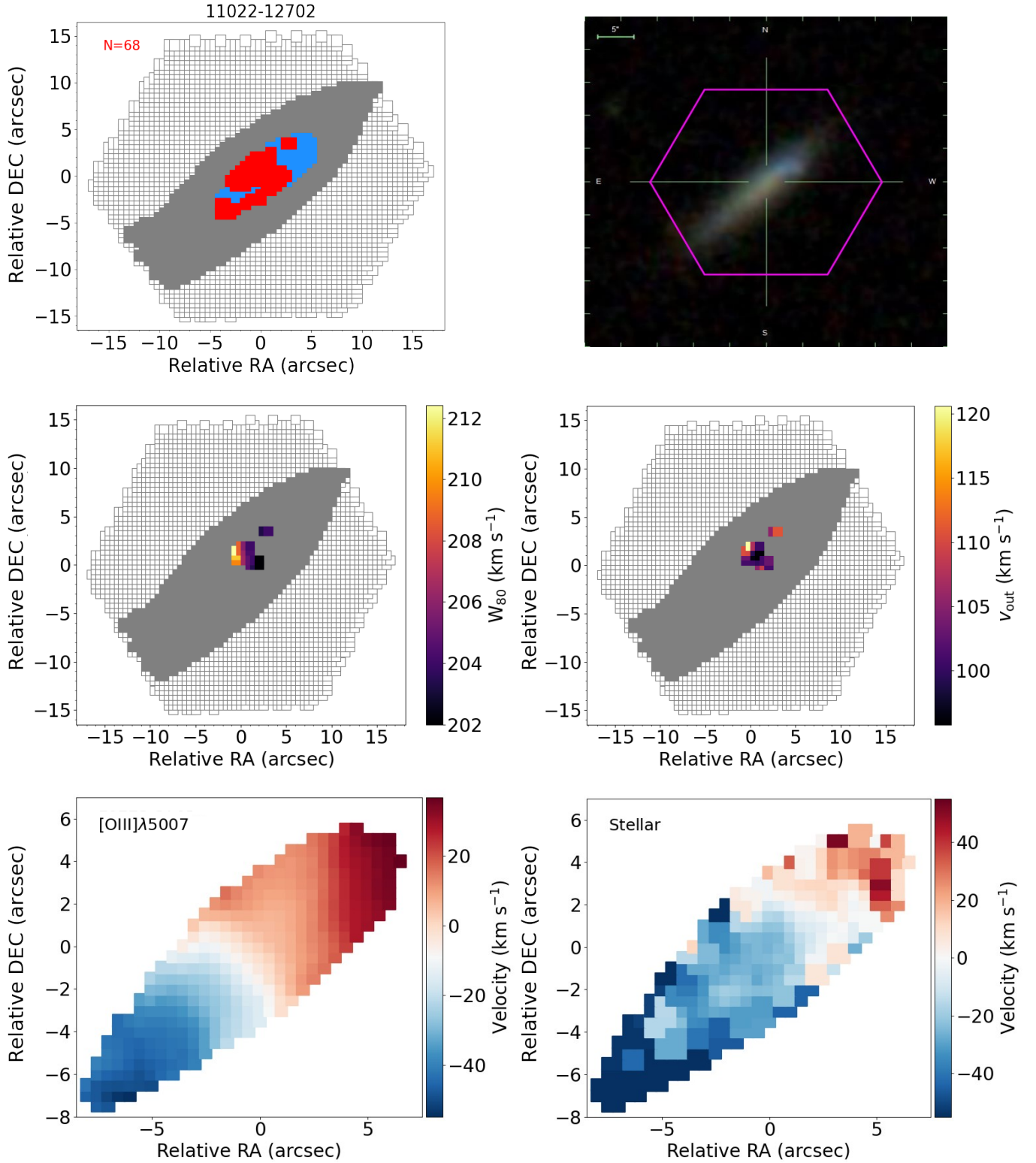


Fig. B.2: Same caption as in Fig. 2 for the dwarf galaxy 11022-12702.

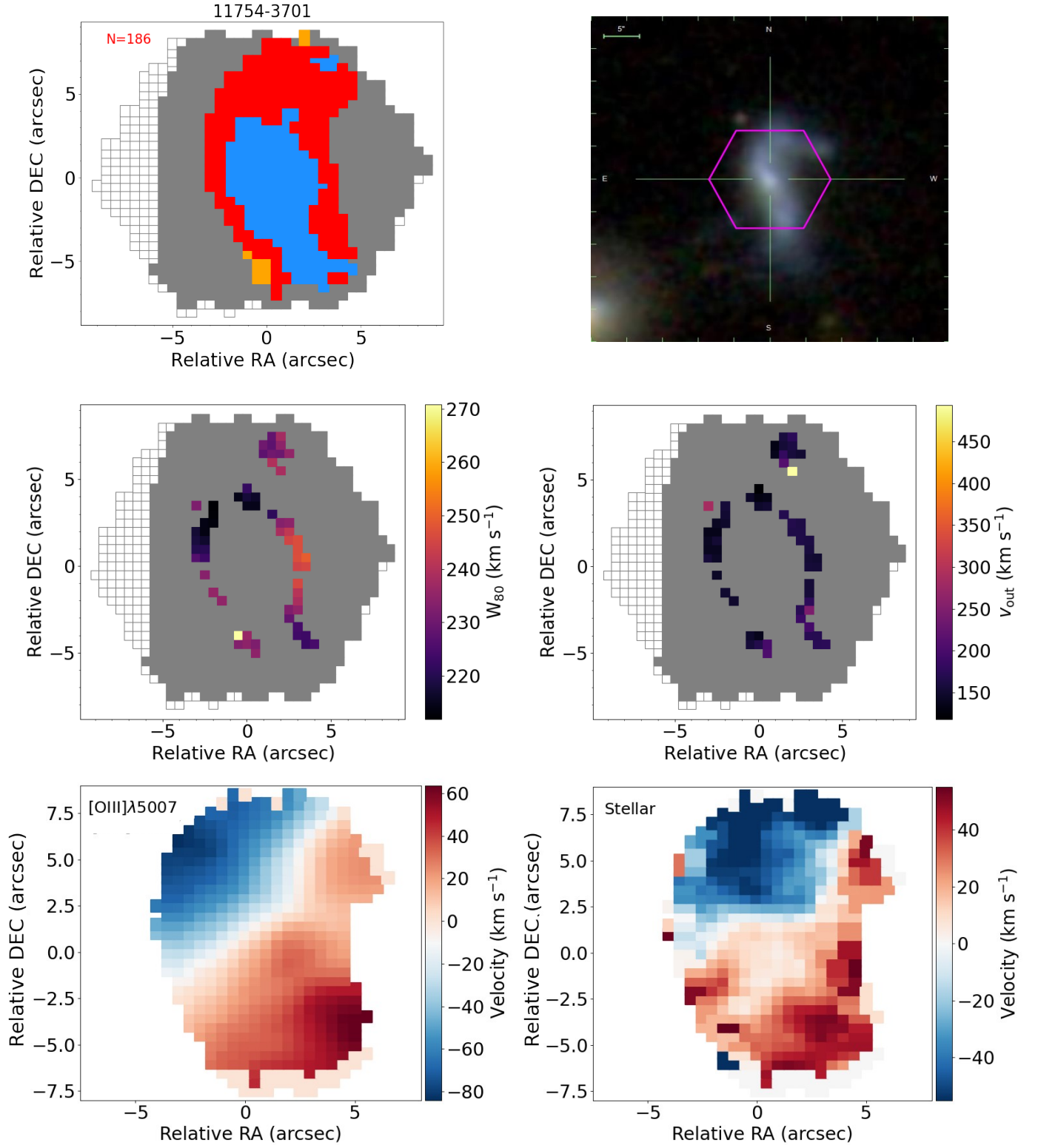


Fig. B.3: Same caption as in Fig. 2 for the dwarf galaxy 11754-3701.

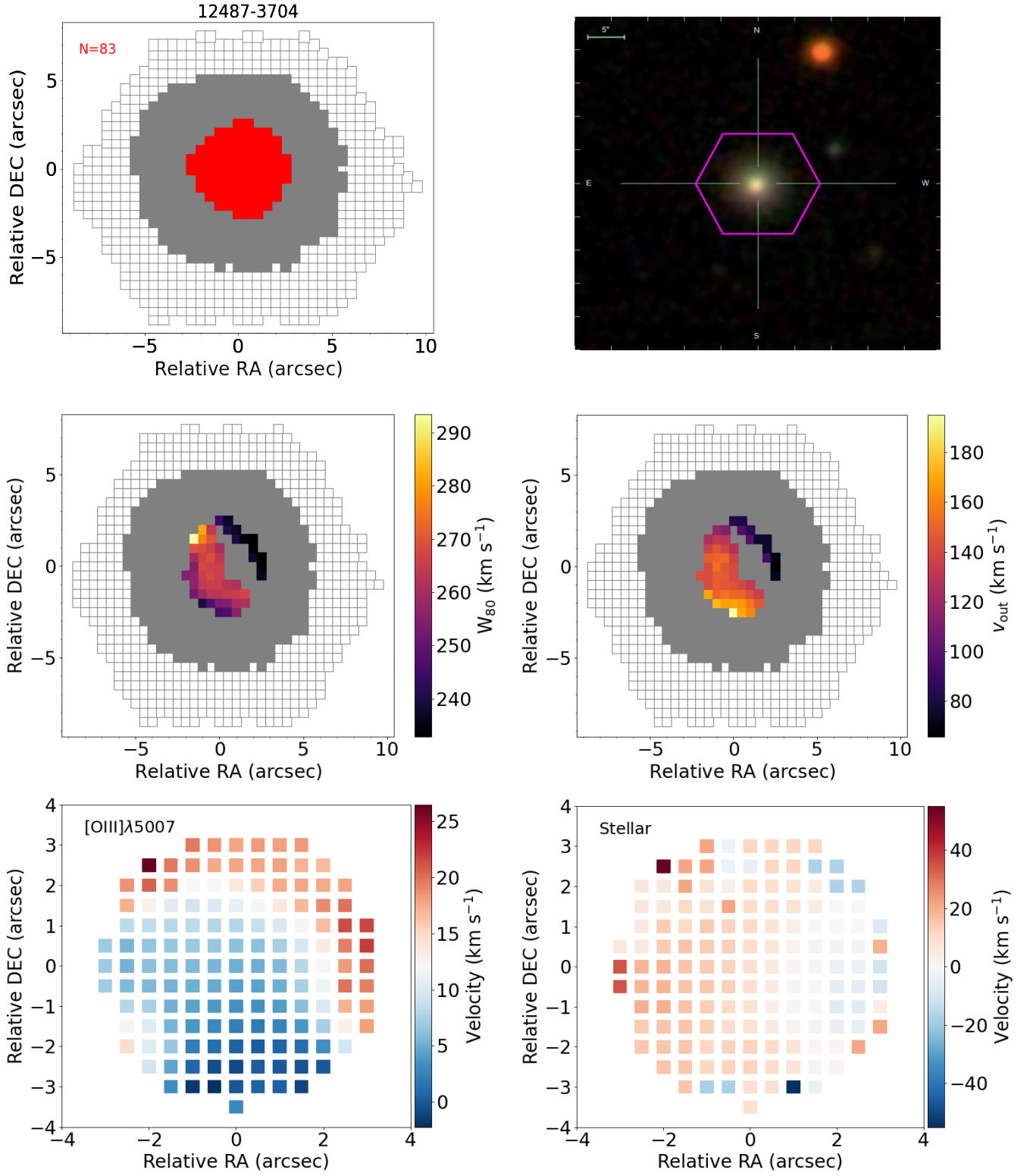


Fig. B.5: Same caption as in Fig. 2 for the dwarf galaxy 12487-3704.

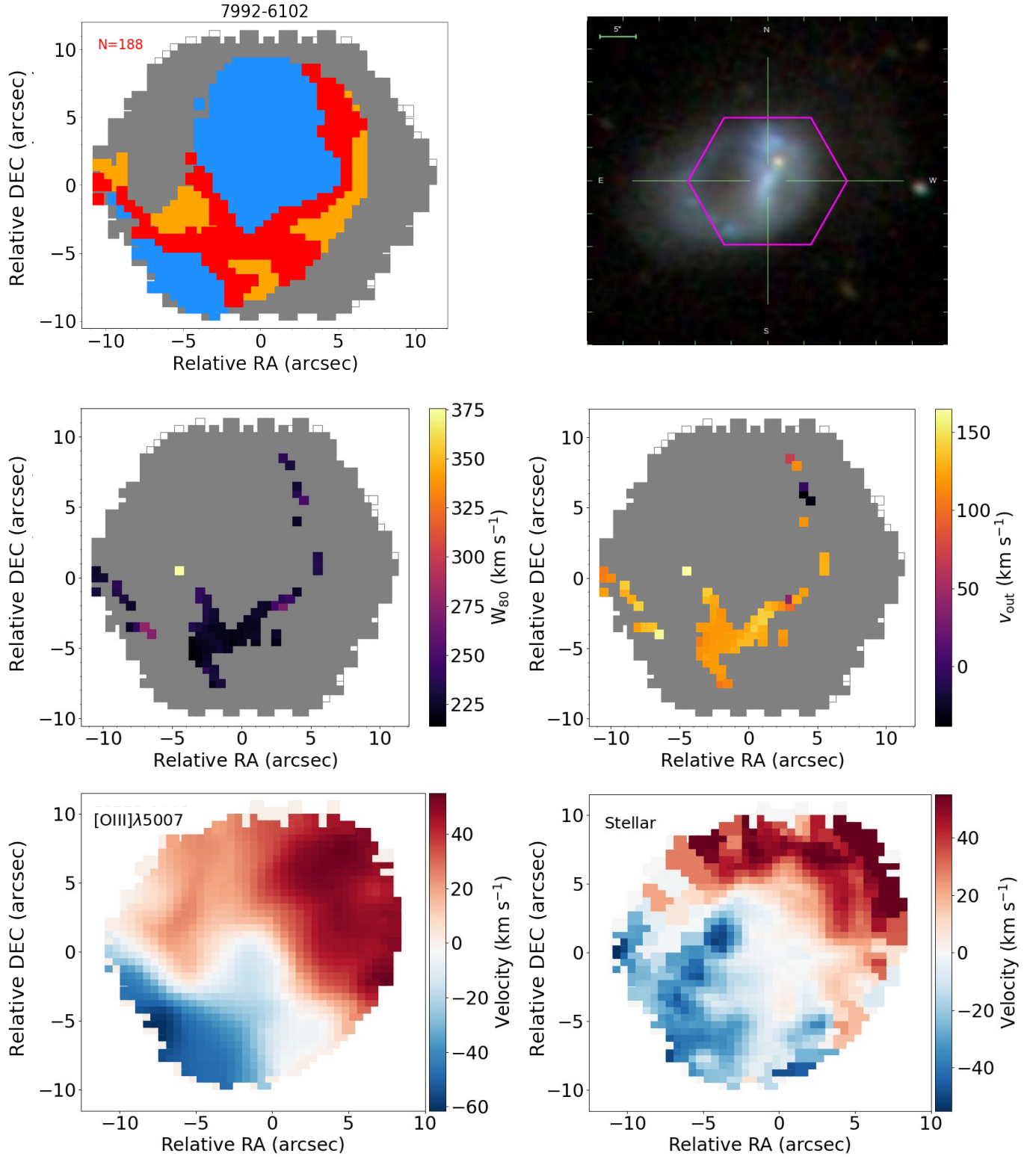


Fig. B.6: Same caption as in Fig. 2 for the dwarf galaxy 7992-6102.

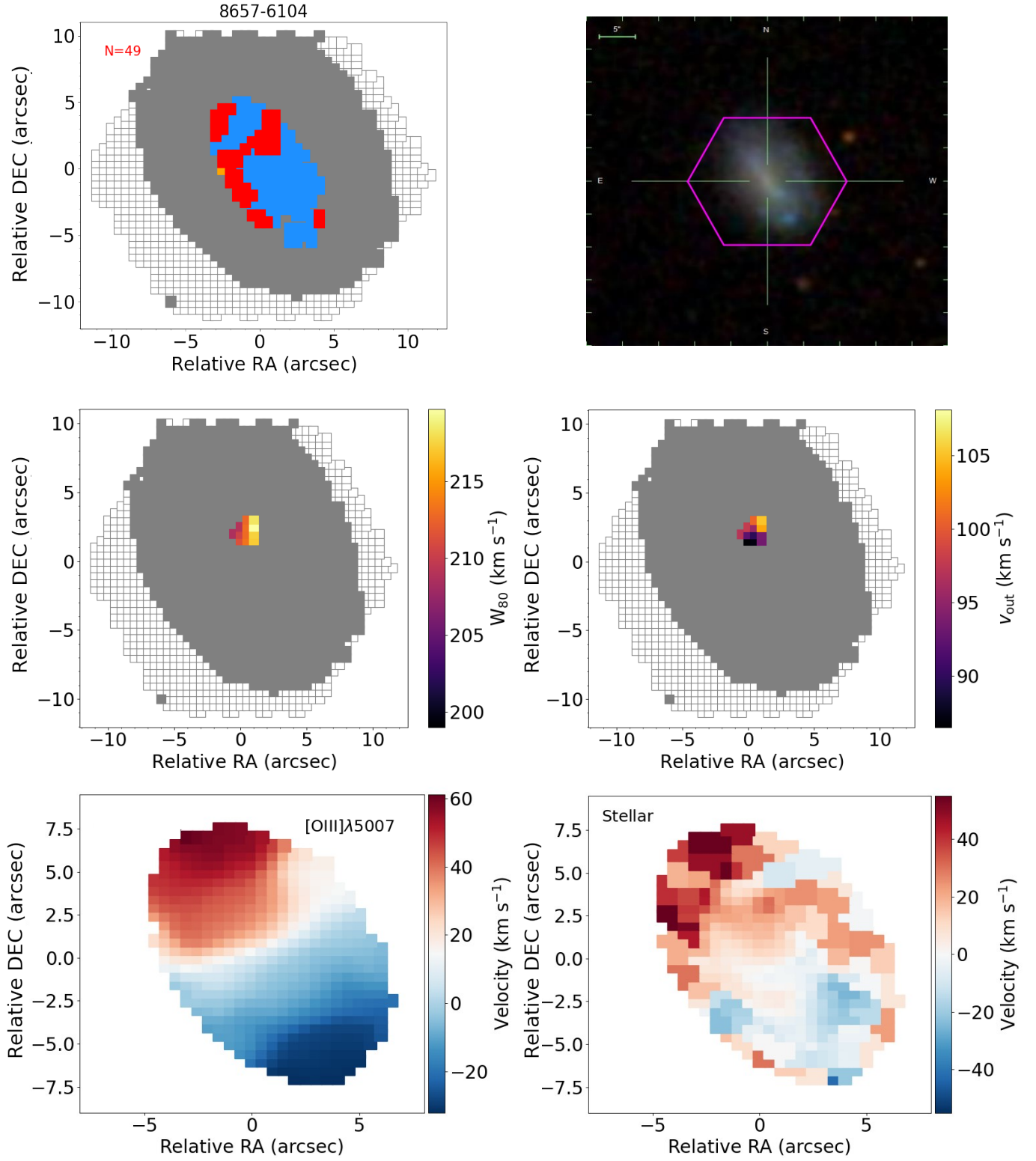


Fig. B.7: Same caption as in Fig. 2 for the dwarf galaxy 8657-6104.

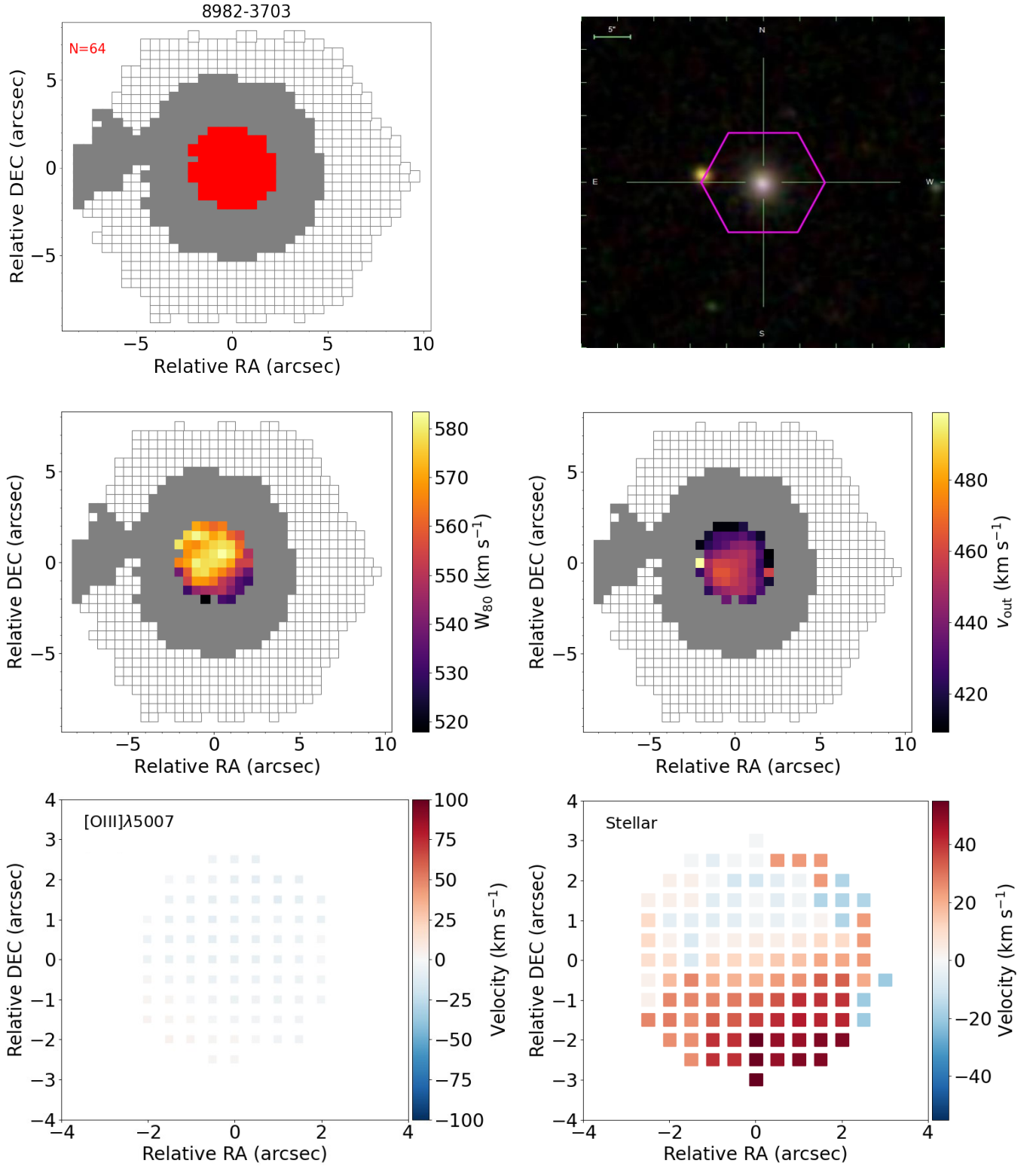


Fig. B.8: Same caption as in Fig. 2 for the dwarf galaxy 8982-3703.

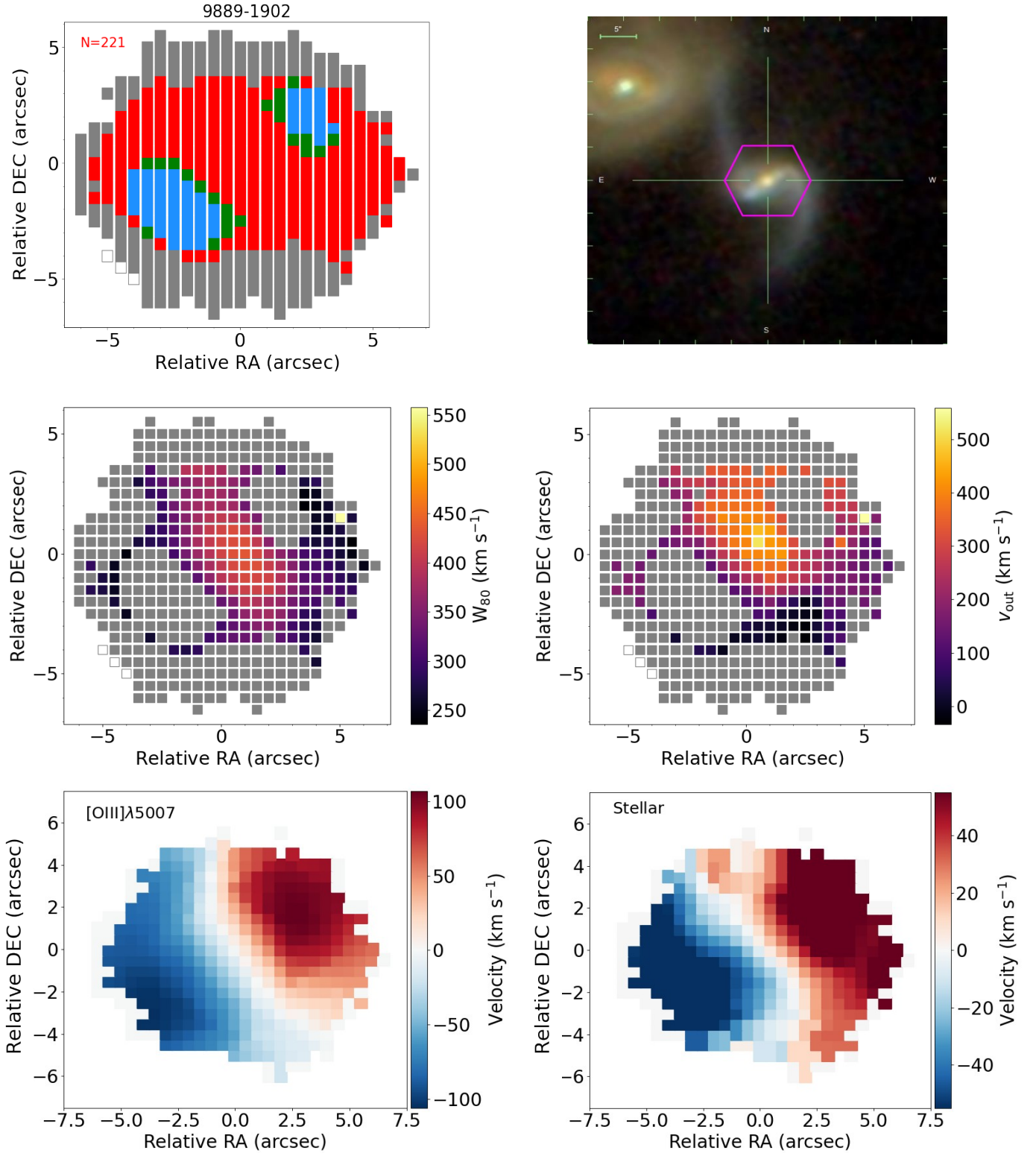


Fig. B.9: Same caption as in Fig. 2 for the dwarf galaxy 9889-1902.